

# Topology and build orientation optimization for additive manufacturing considering build height and overhang area

Luke Crispo<sup>1</sup>, Il Yong Kim<sup>1</sup>

<sup>1</sup>Department of Mechanical and Materials Engineering, Queen's University, 130 Stuart St., Kingston, Ontario, K7L 3N6, Canada

## Correspondence

Il Yong Kim: [kimiy@queensu.ca](mailto:kimiy@queensu.ca)

## Abstract

Simultaneous topology and build orientation optimization approaches aim to reduce the cost of additive manufacturing components by minimizing or eliminating overhanging surfaces and support structure volume. However, current methods do not consider build height, which influences additive manufacturing printing time and can vary significantly based on orientation. This paper presents a topology and build orientation optimization approach that considers both overhanging area and build height during optimization to more accurately model additive manufacturing cost. Gradient-based optimization is performed using a novel build height calculation method and an overhang area formulation that is applicable to additive manufacturing processes that print either on a raft or directly on the build plate. A technique is proposed to automatically initialize build orientation design variables to avoid poor convergence behaviour. The functionality of the approach is verified on two 3D academic models, with optimization results highlighting a clear trade-off between overhang area and build height. Slicer verification of optimized results yielded up to a 27% reduction in print time for fused deposition modelling by simultaneously considering overhang area and build height rather than only optimizing for overhang area.

**Keywords:** Additive manufacturing, Build orientation optimization, Build height, Overhang angle, Topology optimization

## 1 Introduction

Additive manufacturing (AM) has the potential to play an important role in the development of lightweight, highly optimized designs for aerospace and automotive industries. The layer-by-layer AM process enables the generation of highly complex parts with improved performance, that could not be fabricated using traditional manufacturing methods. If AM adoption can result in even a small decrease in overall weight, significant reductions in energy use and greenhouse gas emissions can be achieved over the lifetime of a fleet of vehicles (Huang et al. 2016). However, widespread adoption of AM through industry has not yet been realized, in part due to the increased cost of AM and the need for a complete redesign of traditional components to leverage AM's strengths and account for its limitations.

Topology optimization (TO) is a computational tool, well-suited for AM, that determines an optimized material distribution of a component to minimize an objective function subject to specified constraints. Density-based TO approaches, outlined by Bendsoe and Sigmund (Bendsoe and Sigmund 2003), specify a set of designable elements within

a finite element (FE) model, and use continuous design variables ranging from zero (void) to one (solid) to define an optimized structure. Topology optimization theory has advanced since its inception (Deaton and Grandhi 2014) and has been applied to a variety of practical design problems in the aerospace (Zhu et al. 2016) and automotive (Yang et al. 2000) industries.

While it is possible to print nearly any component using AM, cost driving factors are very different from traditional manufacturing methods and a new Design for Additive Manufacturing (DfAM) framework is required to design cost effective parts (Meisel and Williams 2015, Thompson et al. 2016). The three main cost metrics for AM are material use, printing time, and post processing time. These metrics can be linked to associated underlying physical properties, which can be incorporated into topology optimization to reduce cost. These physical driving factors are build height, surface area, volume, overhang area, and support material volume (Ryan and Kim 2019, Olsen and Kim 2020). Any reduction in these factors can help to make AM a more feasible option for industry, where cost is often a bottom-line consideration.

There has been a significant interest in integrating DfAM considerations into TO in the last 10 years (Liu et al. 2018), with research topics including reduction of AM cost (Ryan and Kim 2019), build orientation optimization (Langelaar 2018), removal of internal voids (Liu et al. 2015), design of infill structure (Schmitt and Kim 2021), and part consolidation (Crispo and Kim 2021). The physical driving factors most frequently implemented into TO are overhang area and support structure volume, as they contribute to all cost factors (material use, printing time, and post processing time). Overhanging surfaces have an angle less than a defined self-supporting threshold angle for the AM process and require support structures to be printed successfully. Support structure and overhang TO methodologies can be broadly classified under two categories:

1. **Self-supporting optimization** aims to completely remove support structure from the design. Overhanging surfaces are identified instead of directly calculating support structure volume. Overhanging surfaces are prevented through either a strict constraint or various projection schemes that prevent unprintable elements from forming.
2. **Support structure optimization** aims to reduce support structure volume without completely prohibiting it from the design. Support structure volume is typically calculated and included in the TO problem statement as an objective or constraint.

### 1.1 Self-Supporting Optimization

Gaynor and Guest proposed a self-supporting TO methodology that detected overhanging surfaces based on elements in a supporting neighborhood and prevented overhangs from developing using a projection scheme (Gaynor and Guest 2016). Langelaar proposed an AM filter that identified printable elements based on a supporting region and excluded unprintable density from the structural analysis, forcing the optimizer to generate a self-supporting structure (Langelaar 2016b). Van de Ven et al. also applied a filtering operation to enforce a printable design, using a font propagation technique for detecting overhanging elements (van de Ven et al. 2020).

Instead of integrating overhanging restrictions using a projection scheme as described above, overhanging surface has also been enforced as a constraint in the optimization problem statement. Qian proposed a density-gradient based approach for calculating overhanging elements and controlled the overhanging angle of optimized designs through an overhanging projected perimeter constraint (Qian 2017). In the same work, Qian also presented a projected undercut constraint that indirectly reduced support structure volume. Various AM constraint functions have been developed for TO problem statements to produce self-

supporting designs based on spatial gradient approximations (Garaigordobil et al. 2018, Zhang et al. 2019, Zhang et al. 2022), Langelaar's AM filter (Kuo and Cheng 2019, Liu et al. 2021, Zou et al. 2021), or self-weight of the AM process (Allaire et al. 2017). Self-supporting requirements have also been integrated into non-density based TO approaches, such as a truss-ground structure (Mass and Amir 2017), movable morphable components and voids frameworks (Guo et al. 2017, Zhang and Zhou 2018), and level set TO approaches (Wang et al. 2018), all of which enforce a support structure free design.

### 1.2 Support Structure Optimization

Contrary to the previously discussed approaches, Mirzendehdel and Suresh explicitly calculated support structure volume in a level-set TO approach as a function of the surface angle and height of the geometric boundaries, with total support structure volume used as an optimization constraint (Mirzendehdel and Suresh 2016). Langelaar proposed a TO methodology that introduced element-level design variables for part density and support structure density, and minimized a multi-objective problem statement including compliance, overhanging elements, and support structure volume (Langelaar 2016a). Ryan and Kim (Ryan and Kim 2019), Sabiston and Kim (Sabiston and Kim 2019), and Mhapsekar et al. (Mhapsekar et al. 2018) calculated support structure volume by assuming linear supports from all overhanging surfaces and optimized part geometry for the weighted sum objective of compliance and support structure volume. Xu et al. calculated linear support structures and instead solved the TO problem for various support structure constraint limits (Xu et al. 2020).

Support structure volume has also been considered indirectly by adjusting the element stiffness penalty function based on an element's support condition (Ranjan et al. 2017) and by minimizing the weighted sum of compliance and a penalty function that represented the cost of deviating from a self-supporting design, with a larger penalty on higher overhanging elements (Thore et al. 2019).

### 1.3 Build Orientation Optimization

The previously mentioned DfAM TO approaches consider a fixed build orientation selected either a priori or arbitrarily. However, for a given structure, some build orientations may require significantly less support structure, meaning fewer changes are needed to reduce overhanging surfaces. When generating a self-supporting design, the selected build orientation can result in a 9 – 16% difference in compliance of the optimized design (Gaynor and Guest 2016, Langelaar 2016b). The selection of an ideal build orientation is often intuitive for academic 2D models, especially when the

baseline optimized geometry is known in advance, but can be challenging for complex 3D problems.

Olsen and Kim (Olsen and Kim 2020) and Fritz and Kim (Fritz and Kim 2020) developed multi-objective problem statements to minimize compliance and support structure volume as a function of element density and build orientation design variables. Wang and Qian simultaneously optimized build orientation and part topology with the addition of two overhang constraints for internal and external supports (Wang and Qian 2020). Wang extended this method to enforce self-supporting features only in enclosed voids (Wang 2022), while Chen et al. extended this approach to consider part segmentation using a neural network (Chen et al. 2023). Wang et al. proposed a B-spline parameterized density method for simultaneous build orientation and topology optimization to produce self-supporting designs (Wang et al. 2022). These approaches found that the build orientation design variable may converge to poor local minima depending on the initial build direction vector. To address this concern, some papers repeated the optimization process for multiple initial build orientations and the best optimization result was selected. While this reduces the risk of converging to a poor local minimum, it is very dependent on the initial orientation selected. If many initial orientations are used to avoid this issue, then a large portion of computing time is essentially wasted on optimizations that are eventually discarded.

Langelaar extended previous approaches to simultaneously design part geometry and support structure for multiple preselected build orientations using a smooth minimum function (Langelaar 2018). The optimization process produced an initial geometry that promoted reduced support structure in all orientations, with poor performing orientations gradually removed as the optimization converged, until a single orientation was selected and the component was optimized accordingly. This process is dependent on the number of initial orientations selected, does not explicitly calculate AM printability as a function of orientation, and would have a quadratic increase in starting orientations if implemented for 3D problems.

Build orientation has also been optimized for fixed-geometry components to minimize residual stress (Cheng and To 2019), surface roughness (Delfs et al. 2016), base width (Leary et al. 2014), and volumetric error (Matos et al. 2020), however these criteria are outside the scope of this research.

#### 1.4 Build Plate Identification

The fixed-orientation DfAM TO algorithms discussed above (except for (Ryan and Kim 2019), (Sabiston and Kim 2019) and (Allaire et al. 2017)) dictate that the part must

build upwards from the bottom of the design space. In most numerical verification models presented in these approaches, the build orientation was selected such that the design space was laid flat on the build plate. However, it is unclear how this approach would behave if the build orientation was rotated to a non-principal angle as shown in Figure 1 (A). Either the entire bottom edge would be incorrectly defined as self supporting, or the structure would be forced to build up from the bottom corner of the design space. In this example, it is evident that the build plate could simply be raised up towards the bottom of the part to avoid this issue. This also occurs in select numerical examples, such as the tension beam in Figure 1 (B). Zou et al. demonstrated that requiring the part to build up from the bottom of the design space caused a 7% - 89% increase in compliance, depending on the optimization parameters (Zou et al. 2021). In this model, the baseline design is very close to being self-supported if the build plate were to be raised. While the authors note that this academic model is used to test the capacity of the proposed methods, this example also illustrates a limitation of the self-supporting approaches. In complex problems, especially for 3D design spaces that are not aligned with the principal axes, a fixed build plate location building from the bottom of the design space can artificially constrain the geometry, potentially resulting in inferior performance.

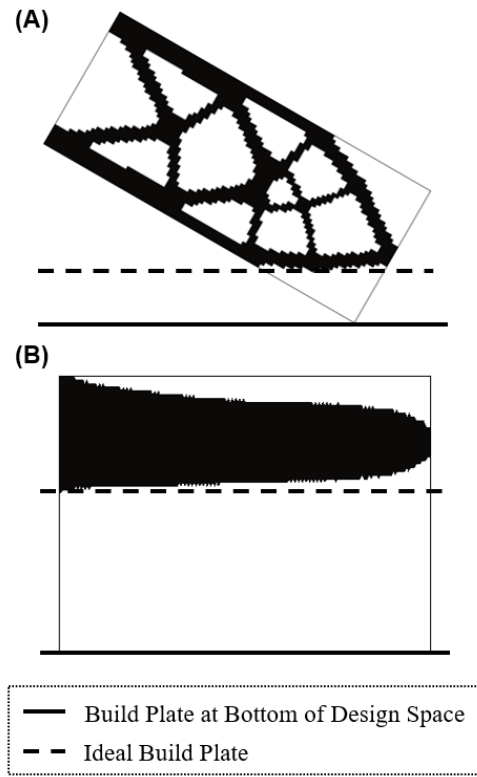


Figure 1 Sample TO results of (A) cantilever beam and (B) tension beam problems, highlighting potential issues when building from the bottom of the design space.

These fixed-orientation approaches also assume that the bottom of the part is printed directly on the build plate, shown in Figure 2 (A), which is valid for fused deposition modelling (FDM). However, in other AM methods, such as stereolithography (SLA) or powder bed fusion (PBF), the component is instead printed on a raft. A raft, shown in Figure 2 (B), consists of a few layers of support structure between the bottom surface of the component and the build plate that helps with adhesion (among other things). Components requiring a raft will have additional support structure volume and an additional overhanging surface, both of which ultimately increase cost. The geometry and orientation of a component influences the area of the raft; however, this is not accounted for in fixed-orientation optimization approaches. Another important distinction between these two categories is that it is impossible to eliminate all overhangs and support structure when printing on a raft because the geometry must build up from at least one point.

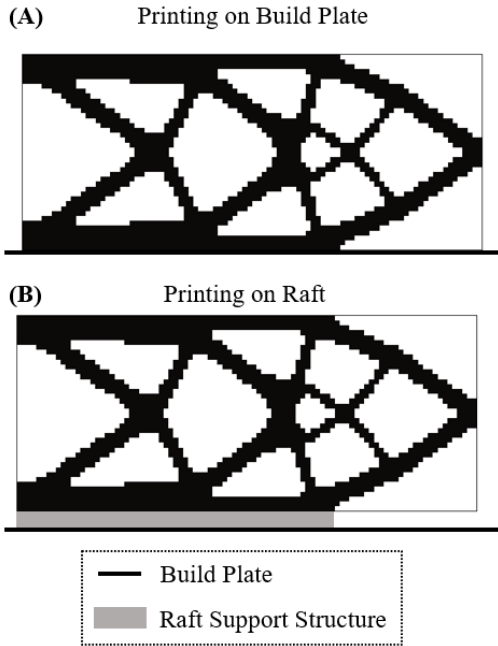


Figure 2 Sample cantilever beam structure comparing (A) printing directly on the build plate and (B) printing on a raft.

The previously discussed topology and build orientation optimization methods adjust the build plate based on the orientation of the component; however, these methods (expect for (Wang et al. 2022)) assume the component is printed on a raft. These approaches therefore calculate all surfaces, including the external bounds of the design space to be overhanging, and are not valid for AM processes that print on the build plate. Wang et al. (Wang et al. 2022) instead excluded a narrow-band region at the bottom boundary of the part from the overhang constraint, but this adjustment was not incorporated in a smooth and differentiable function.

Therefore, this method did not consider the effect of changing build plate location in the sensitivity expressions, which can have a significant impact on build orientation design variable sensitivities to align flat faces of the structure with the build plate.

### 1.5 Build Height Optimization

When optimizing build orientation to reduce support structure and overhanging surfaces, the result often converges to a tall thin structure. This effect is more prevalent in geometries with long rectangular design spaces, such as the cantilever and Messerschmitt-Bolkow-Blohm (MBB) beam problems (Langelaar 2018, Fritz and Kim 2020, Olsen and Kim 2020, Wang and Qian 2020). These designs result in a large build height, which affects the number of layers that must be printed and is generally associated with an increase in printing time (Gao et al. 2015, Ranjan et al. 2017). This is because a dwell time is needed during printing to prepare the machine for each new layer. In powder and liquid resin-based AM processes, the dwell time can significantly contribute to the overall printing time. In addition to the increase in cost, these tall and thin structures also often have only one or two attachment points to the build plate and may fail during printing due to warping or deformation.

Liu et al. minimized a multi-objective sum of build height and support structure volume in a level set TO approach for a fixed orientation (Liu et al. 2019). The potential build height reductions that can be achieved through this work are limited because orientation typically has a more significant influence on height compared to component geometry. Zhou et al. considered build volume constraints (length, width, and height) in a multi-component TO approach to divide a structure into printable parts, but did not minimize height as an optimization objective or consider rotation of the build volume (Zhou et al. 2019). Build height has been optimized with respect to orientation for fixed geometry components using genetic algorithms (Pandey et al. 2004, Phatak and Pande 2012) and other optimization tools (Leary et al. 2014, Delfs et al. 2016, Zhang et al. 2017, Matos et al. 2020). However, build height has never been considered in simultaneous build orientation and topology optimization, where there is an important trade-off between support structure and height.

### 1.6 Knowledge Gap and Objectives

Despite its contribution towards printing time and ultimately the cost of a component, build height has never been integrated into a TO problem statement as a function of build orientation design variables. There is an unexplored trade-off between build height and support structure costs, especially when selecting the optimal build orientation, that

should be considered when designing a component for AM. Instead, existing topology and build orientation optimization approaches may inadvertently increase print time by selecting orientations with a large build height.

An effective method has not been proposed for initializing orientation design variables in topology and build orientation optimization for 3D problems. The design problem can be subject to many poor local minimum orientations, especially when considering potentially conflicting objectives such as build height and support structure. Repeating the optimization process with various initial orientations is computationally expensive and does not guarantee convergence to a good orientation. Alternatively, Langelaar's simultaneous orientation optimization process is limited to the selected starting orientations and does not inherently optimize build orientation as a design variable.

Existing approaches in literature are formulated for either 1) printing directly on the build plate or 2) printing on a raft; ultimately limiting their applicability to select AM processes. Fixed orientation methods are typically formulated for printing on the build plate at the bottom of the design space (with unknown implications for non-principle build directions), while topology and build orientation optimization methods are typically formulated for printing on a raft. No topology and build orientation optimization method has been formulated for printing on the build plate as a differentiable function, which has complex behavior when considering component rotation.

The objective of this paper is to develop a methodology for simultaneous build orientation and topology optimization to minimize AM cost by considering the trade-off between build height and overhang area. To accomplish this, build height is calculated as a smooth and continuous function of topology and build orientation design variables. Overhang area calculation is formulated for printing both on the build plate or on a raft, through a smooth and differentiable build plate identifier field. In addition, a new automatic build orientation initialization scheme is presented to reduce the likelihood of converging to a poor orientation in 3D problems. The proposed approach is applied to two academic models and the print time and material usage savings are verified using a slicer software.

## 2 Methodology

The proposed simultaneous build orientation and topology optimization method solves the problem statement shown in Equation (1). The multi-objective function  $J$  represents a weighted sum of structural compliance  $C$  and two AM physical cost driving factors: build height  $H$  and overhang area  $\Psi$ . Overhang area is minimized instead of a strict

constraint or projection scheme to avoid overly restricting the problem by enforcing a fully self-supporting design. A fully self-supporting design may result in an undesirable compliance increase, whereas a multi-objective approach instead allows the designer to vary the relative importance of compliance and AM cost objectives through the  $w_1$  and  $w_2$  weighting factors. This formulation can therefore achieve a range of designs with various reductions in overhang area and associated increases in compliance, which is not possible with projections schemes or strict overhang constraints. While the AM objectives can also be implemented as constraints, it is challenging to determine appropriate constraint limits because the magnitude of these physical cost driving factors may not have an inherent significance on the design problem. The multi-objective approach is also better suited for design exploration because it inherently considers the trade-offs between individual AM responses to minimize the overall objective, which is more challenging when specifying individual constraint limits for each AM metric. In addition, the incorporation of constraints can have implications on convergence behavior, sometimes requiring continuation schemes to achieve high quality results. While not included in the manuscript, the proposed approach was also implemented with build height and overhang area constraint functions, achieving similar behaviour to the numerical results shown.

$$\begin{aligned} \min J(\underline{x}, \theta) &= w_1 \frac{C(\underline{x})}{C_0} + (1-w_1) \left( w_2 \frac{H(\underline{x}, \theta)}{H_0} + (1-w_2) \frac{\Psi(\underline{x}, \theta)}{\Psi_0} \right) \\ \text{s.t. } \underline{K}\underline{u} &= \underline{f} \\ g(\underline{x}) &= \frac{V(\underline{x})}{V_{DS}} \leq \bar{V} \\ 0 \leq x_e &\leq 1, \quad e = 1, \dots, N \\ -180^\circ < \theta_1 &\leq 180^\circ \\ -90^\circ < \theta_2 &\leq 90^\circ \end{aligned} \quad (1)$$

The compliance, build height, and overhang area are normalized by  $C_0$ ,  $H_0$ , and  $\Psi_0$ , respectively, to ensure similar magnitudes between the objectives. The structure is subjected to a linear static governing equation, where  $\underline{f}$  is the input vector of applied loads,  $\underline{K}$  is the global stiffness matrix based on the geometry, and  $\underline{u}$  is the resultant vector of nodal displacements. The optimization is constrained to a volume fraction limit of  $\bar{V}$  through a mass fraction constraint  $g$  defined by the ratio of the component volume  $V$  to the volume of the design space  $V_{DS}$ . The geometry is defined through the element density design variable vector  $\underline{x}$  with a length of  $N$  and the build orientation is defined through the orientation design variable vector  $\theta$  with a length of two for 3D problems.

## 2.1 Topology Optimization Formulation

Element density design variable values are filtered to avoid numerical checkerboarding (Sigmund 2007) and to provide a smooth density field for the spatial gradient calculations that will be required for detecting overhanging elements. The  $e$ -th filtered density  $\tilde{x}_e$  is calculated based on the  $N_e$  neighbouring elements within the filter radius  $R_F$  as

$$\tilde{x}_e = \frac{\sum_{i \in N_e} w_{ei} v_i x_i}{\sum_{i \in N_e} w_{ei} v_i} \quad (2)$$

where  $v_i$  is the volume of the  $i$ -th element. The weighting term is calculated based on the magnitude of the vector between two element centroids as

$$w_{ei} = \max(0, R_F - \| \underline{s}_{ei} \|) \quad (3)$$

$$\underline{s}_{ei} = \underline{r}_e - \underline{r}_i \quad (4)$$

where  $\underline{r}_e$  and  $\underline{r}_i$  are the position of the  $e$ -th and  $i$ -th element centroids, respectively.

The density filtering process results in a layer of intermediate densities around all structural members with a width equal to the filter radius. A more discrete solution can be obtained by projecting the filtered densities towards 0/1 values using the smooth Heaviside function outlined by Wang et al. (Wang et al. 2011). The resultant physical densities are calculated as

$$\rho_e = \frac{\tanh(\beta_\rho \eta_\rho) + \tanh(\beta_\rho (\tilde{x}_e - \eta_\rho))}{\tanh(\beta_\rho \eta_\rho) + \tanh(\beta_\rho (1 - \eta_\rho))} \quad (5)$$

where the slope of the Heaviside is controlled by  $\beta_\rho$ , which is gradually increased throughout the optimization, and  $\eta_\rho = 0.5$  is the threshold point. The physical densities are used for evaluation of compliance, volume, build height, and overhang area.

Element stiffness is interpolated using the Solid Isotropic Material with Penalization (SIMP) method as

$$E_e(x_e) = E_{\min} + \rho_e^p (E_0 - E_{\min}) \quad (6)$$

where  $p$  is the penalty factor,  $E_0$  is the material Young's Modulus, and  $E_{\min} = 10^{-8} E_0$  is the small, non-zero stiffness of a void element. Compliance is calculated using an external FE solver based on the interpolated element stiffness and component volume is calculated from the physical densities as:

$$V(x) = \sum_{e \in N} \rho_e v_e \quad (7)$$

## 2.2 Build Orientation Optimization Formulation

The build orientation of the component is determined by the build direction vector  $\underline{b}$ , which points in the build direction (i.e., normal to the build plate pointing toward the build volume) and is defined based on rotations of a reference build direction vector  $\underline{\tilde{b}} = \underline{b}(0^\circ, 0^\circ)$  aligned with the positive  $y$  direction as shown in Figure 3 (A). The build direction vector is determined by rotating the reference vector by  $\theta_1$  about the  $z$  axis followed by a rotation of  $\theta_2$  about the  $x$  axis. Only the build direction vector is rotated as a function of the orientation design variables, and the component itself does not rotate in this formulation. For easier visualization of component's orientation on the build plate, the component can be rotated into a new  $\tilde{x}$ - $\tilde{y}$ - $\tilde{z}$  coordinate system where the build orientation vector is always aligned with the  $y$  axis, shown in Figure 3 (B). Only two rotations are needed in this approach because a rotation of the component about its build direction vector, the  $\tilde{y}$  coordinate in Figure 3 (B), does not change the height or overhanging surfaces of the component.

The rotated build direction vector is calculated from the reference build direction vector as

$$\underline{b}(\theta) = \underline{R}\underline{\tilde{b}} \quad (8)$$

$$[\underline{\tilde{b}}] = [0, 1, 0]^T \quad (9)$$

where  $\underline{R}$  is a 3D rotation matrix representing the consecutive  $z$  and  $x$  rotations defined as:

$$[\underline{R}(\theta)] = \begin{bmatrix} \cos \theta_1 & -\sin \theta_1 & 0 \\ \cos \theta_2 \sin \theta_1 & \cos \theta_2 \cos \theta_1 & -\sin \theta_2 \\ \sin \theta_2 \sin \theta_1 & \sin \theta_2 \cos \theta_1 & \cos \theta_2 \end{bmatrix} \quad (10)$$

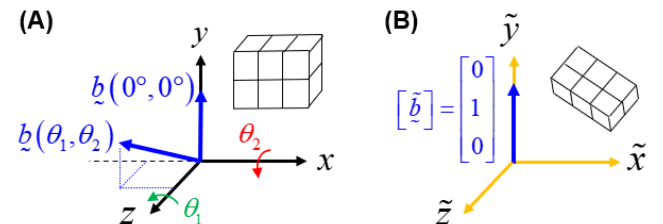


Figure 3 Formulation of build orientation optimization showing (A) the reference and rotated build direction vector, and (B) the component's orientation on the build plate using a rotated coordinate system.

## 2.3 Build Height Calculation

The build height of an AM component is defined as the largest normal distance from the build plate to any point of the component. The calculation of build height must be carefully formulated to develop a smooth and differentiable

equation in terms of both element density and orientation design variables. Build height is calculated using element centroid positions to allow for integration with any FE software using both structured and unstructured meshes. First, the height of each element in the rotated coordinate system is calculated as

$$h_e(\theta) = \underline{r}_e \cdot \underline{b} \quad (11)$$

where  $\underline{r}_e$  is the position of the  $e$ -th element centroid in the FE model. Conceptually,  $h_e$  is the  $\tilde{y}$  coordinate of the  $e$ -th element in the rotated coordinate system from Figure 3 (B). This is not equivalent to element's distance from the build plate as the build plate is not necessarily located at the  $\tilde{y} = 0$  plane.

After calculating the height of each element, build height can be determined by finding the distance between the uppermost point (or top) of the part and the lowermost point (or bottom) of the part, which corresponds to the build plate location. The uppermost point of the component could be calculated using a smooth maximum function of the  $h_e \rho_e$  term for all elements. This accounts for the topology of the structure by linearly scaling element height towards zero for void elements (as they do not contribute to part height). However, the lowermost point cannot be calculated in this way (for example with a smooth minimum function) because the  $h_e \rho_e$  term is equal to zero for all void elements.

Instead, build height is calculated in this work as the sum of the vertical distance from the centroid to the top of the part  $T$  and the vertical distance from the centroid to the bottom of the part  $B$  as illustrated in Figure 4. By first calculating the height centroid  $\bar{h}$ , smooth maximum functions of each element's vertical distance from the centroid can be used to calculate the top and bottom distances.

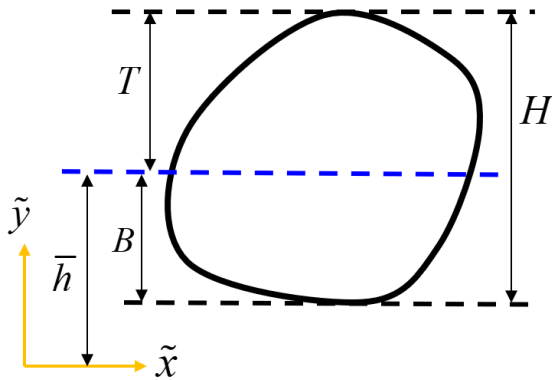


Figure 4 Demonstration of build height calculation for a 2D geometry based on the top and bottom distances from the height centroid.

When multiplying element height by physical densities, intermediate density elements have a significantly reduced

height, and the optimizer can artificially reduce build height by using intermediate density elements at the extremities of the component. Therefore, inverse penalized physical densities  $\rho_e^{1/p}$  are used whenever calculating height, where  $p$  is the SIMP penalty factor, to discourage these intermediate density elements from forming. The height centroid of the part is therefore calculated using a weighted average of element height multiplied by the inverse-penalized density as follows:

$$\bar{h}(x, \theta) = \frac{\sum_{e \in N} h_e \rho_e^{1/p}}{\sum_{e \in N} \rho_e^{1/p}} \quad (12)$$

The vertical distance of each element from the height centroid is also calculated using the inverse-penalized element density as:

$$\hat{h}_e(x, \theta) = (h_e - \bar{h}) \rho_e^{1/p} \quad (13)$$

The calculation of these distances is demonstrated in Figure 5 for a sample 2D intermediate topology result. The element height in (B) increases in the build direction vector shown in (A). Note that element height may be positive or negative depending on the orientation design variables. It is evident that a maximum of the  $h_e \rho_e^{1/p}$  field shown in (C) would accurately identify the top of the part, but the minimum of this field would not identify the bottom, as this field will always be equal to zero for void elements. Instead, the distance term in (D) can be used for identification of the top and bottom distances. This field has a value of zero for void elements and elements that lie along the height centroid indicated by the dotted line. The maximum of this field represents the vertical distance from the centroid to the top of the part, and the minimum of this field represents the vertical distance from the centroid to the bottom of the part.

The vertical distances from the height centroid to the top  $T$  and bottom  $B$  of the part are calculated as

$$T(x, \theta) = S_{MAX}(\hat{h}) \quad (14)$$

$$B(x, \theta) = S_{MIN}(\hat{h}) \quad (15)$$

where  $S_{MAX}(\zeta)$  and  $S_{MIN}(\zeta)$  are smooth maximum and minimum functions, respectively. The smooth maximum/minimum function of an arbitrary input vector  $\zeta$  of length  $N$  is defined as

$$S(\zeta) = \frac{\sum_{i \in N} c_i e^{\alpha c_i}}{\sum_{i \in N} e^{\alpha c_i}} \approx \begin{cases} \max(\zeta), & \alpha > 0 \\ \min(\zeta), & \alpha < 0 \end{cases} \quad (16)$$

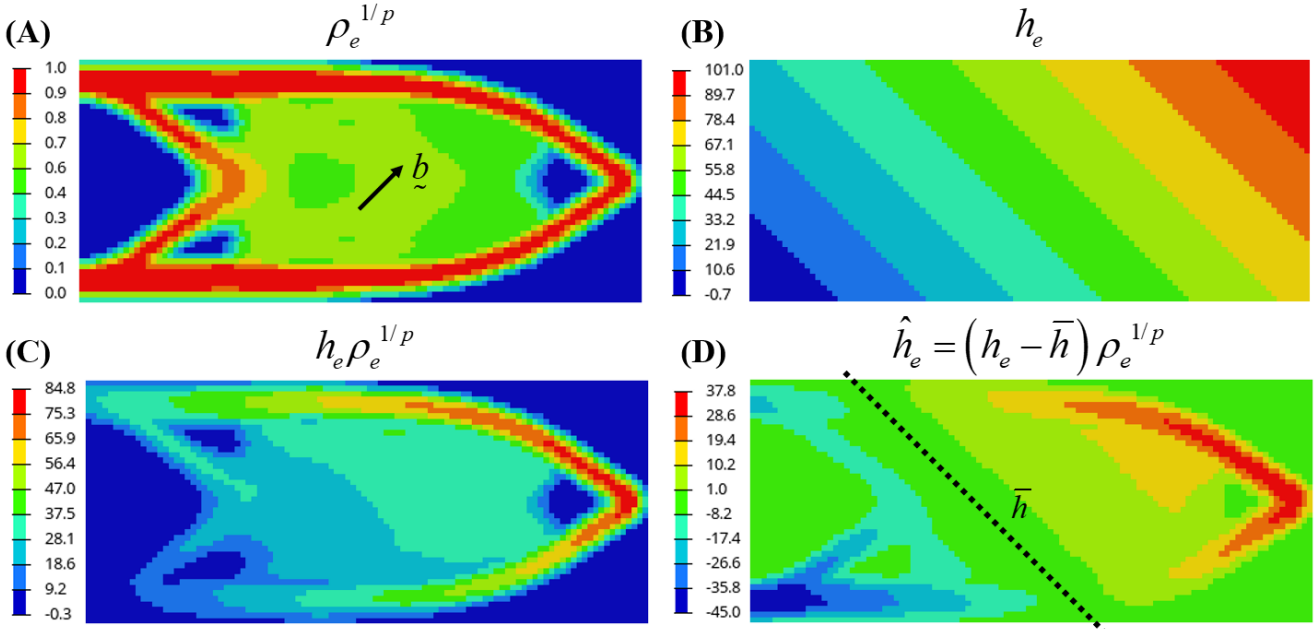


Figure 5 Element height terms used in build height calculation for an intermediate 2D topology optimization result in (A) printed in the indicated build orientation. Element height is plotted in (B) and multiplied by element density in (C). The height centroid is indicated in (D) along with a plot of element distance from the centroid.

where the scaling factor  $\alpha$  adjusts the smoothness of the approximation, approaching a true maximum/minimum as the magnitude of the scaling factor increases. In this work, values of  $\alpha = 100$  and  $\alpha = -100$  were used for the smooth maximum and minimum functions respectively, as this provided reasonable height approximations while maintaining smooth differentiability during optimization. It should be noted that numerator and denominator terms in Equation (16) become exceedingly large for large values of  $\alpha$ , which can lead to numerical overflow. Element height can be linearly scaled to values between zero and one before all calculations to mitigate this issue.

The build height of the component used in the optimization objective function is then calculated by adding the top and bottom distances as follows:

$$H(x, \theta) = T - B \quad (17)$$

Sensitivities of the build height calculation with respect to element density and orientation design variables are presented in Appendix A.

## 2.4 Overhang Area Calculation

The spatial gradient of the physical density field can be used to identify boundaries and overhanging features of a topology optimization solution as presented in detail by Qian (Qian 2017). The spatial gradient vector is calculated using element centroid positions for any unstructured FE mesh by modifying the approach from Crispo et al. (Crispo et al. 2021) to mimic an extended Sobel operator (Kekre and Gharje 2010) with an increased filter radius as:

$$\nabla \rho_e(x) = \frac{\sum_{i \in N_e} v_i \rho_i \xi_{ei}}{\sum_{i \in N_e} \|\xi_{ei}\| v_i} \quad (18)$$

Equation (18) determines the vector from the  $e$ -th element to the density centroid of its neighbouring elements within an interface radius  $R_I$ . This vector represents the spatial gradient and is normalized through the denominator term to provide similar magnitudes across problems with varying element sizes. The spatial gradient vector  $\nabla \rho_e$  has a length of three for 3D problems, representing the change in physical density in each of the principal directions.

The magnitude of the spatial gradient vector can be calculated as

$$\|\nabla \rho_e\| = \sqrt{\sum_{j=1}^3 (\nabla \rho_e)_j^2 + \varepsilon^2} - \varepsilon \quad (19)$$

where  $j$  is the spatial direction and  $\varepsilon = 0.01$  is a small number that provides a smooth magnitude calculation. Elements on the boundary of component topology will have a relatively high spatial gradient magnitude due to the transition between solid and void density, while elements in solid or void regions will have a relatively small spatial gradient magnitude. A measure of an element's contribution to the overall surface area of a part can be calculated using a modified smooth Heaviside function as

$$\phi_e(\rho) = \frac{v_e^{2/3}}{a} \frac{\tanh(\beta_\phi \eta_\phi) + \tanh(\beta_\phi (\|\nabla \rho_e\| - \eta_\phi))}{2 \tanh(\beta_\phi \eta_\phi)} \quad (20)$$

where  $\beta_\phi$  is the slope of the function that is gradually increased throughout optimization, and  $\eta_\phi = 0.1$  is horizontal shift of the function. Equation (20) uses a new smooth Heaviside function because the function presented in Equation (5) is specifically formulated for topology optimization and passes through the points  $(0,0)$  and  $(1,1)$  as input values always range between zero and one. This modified smooth Heaviside function is useful for thresholding small positive input values as it passes through the points  $(0,0)$  and  $(2\eta_\phi, 1)$ . The element surface area calculation also uses the element volume  $v_e$  and a normalization term  $a=2$  to scale the Heaviside output to provide a more realistic estimate of the surface area, however these terms can be set equal to one as they simply scale the surface area magnitude.

Overhanging surfaces are identified by comparing the orientation of a component boundary relative to the self-supporting threshold angle of selected AM process. The angle  $\alpha_e$  between the boundary's spatial gradient calculated in Equation (18) and the rotated build direction vector is used for this comparison, as outlined by Ryan and Kim (Ryan and Kim 2019). An element is identified as overhanging if this angle  $\alpha_e$  is less than the self-supporting threshold angle  $\alpha_e < \bar{\alpha}$ . This can be more easily calculated by identifying an overhanging element if  $\cos \alpha_e > \cos \bar{\alpha}$ , calculating the cosine of this angle in Equation (21). The  $\varepsilon$  term is added to the denominator to avoid dividing by zero for elements with a spatial gradient equal to zero.

$$\cos \alpha_e(\rho, \theta) = \frac{\nabla \rho_e \cdot b}{\|\nabla \rho_e\| + \varepsilon} \quad (21)$$

An element's overhang indicator can be calculated using a second modified smooth Heaviside function in Equation (22) where the threshold shift is set to  $\eta_\psi = \cos \bar{\alpha}$ , and the slope is set to  $\beta_\psi = 10$ . This smooth Heaviside is useful for thresholding input values that lie between positive and negative one, such as in the cosine function, as it passes through the points  $(-1,0)$  and  $(1,1)$ . This overhang indicator yields a value close to one for overhanging elements and a value of close to zero for elements that do not require support.

$$\psi_e(\rho, \theta) = \frac{\tanh(\beta_\psi (1 + \eta_\psi)) + \tanh(\beta_\psi (\cos \alpha_e - \eta_\psi))}{\tanh(\beta_\psi (1 + \eta_\psi)) + \tanh(\beta_\psi (1 - \eta_\psi))} \quad (22)$$

To only consider overhanging elements on the boundaries of the component, overhang area is calculated by multiplying the overhang indicator and the element surface area as

$$\{, \#252\} \psi_e(\rho, \theta) = \bar{\psi}_e \phi_e \mu_e \quad (23)$$

where  $\mu_e$  is an indicator of whether an element exists on the build plate. Elements on or below the build plate have a value close to  $\mu_e = 0$ , while elements above the build plate have a value close to  $\mu_e = 1$ . When using an AM process that requires a raft, this build plate indicator field can be set to  $\mu_e = 1$  for all elements, as any overhanging surface will require support. When using an AM method that does not require a raft, the build indicator is calculated by comparing the vertical distance of each element from the height centroid ( $h_e - \bar{h}$ ) to the vertical distance to the bottom of the part  $B$ . This can be calculated using the smooth Heaviside function in Equation (24), where the slope  $\beta_\mu$  is gradually increased and the threshold  $\eta_\mu$  is gradually decreased throughout the optimization, respectively. The threshold is adjusted so that the base indicator yields a value close to zero at the bottom of the part, rather than a value of 0.5 if the threshold was set to  $\eta_\mu = 0$ .

$$\mu_e(\rho, \theta) = \begin{cases} 1, & \text{raft} \\ \frac{\tanh(\beta_\mu (1 + \eta_\mu)) + \tanh(\beta_\mu (h_e - \bar{h} - B - \eta_\mu))}{\tanh(\beta_\mu (1 + \eta_\mu)) + \tanh(\beta_\mu (1 - \eta_\mu))}, & \text{build plate} \end{cases} \quad (24)$$

The overhang area calculation is depicted in Figure 6 for a sample intermediate TO density field. The base indicator field in (D) shows a smooth representation of elements that lie on the build plate, with a value approaching zero for elements at the bottom of the component and transitioning to a value of one for all other elements. The overhang area field in (E) is a product of the surface area and overhang indicator fields. When printing on the build plate in (F), the overhang area is eliminated from the bottom of the design space.

The total overhang area used in the optimization objective can be calculated as a sum of all element-level overhang area as:

$$\Psi(\rho, \theta) = \sum_e \psi_e \quad (25)$$

For brevity, the derivation of overhang angle sensitivities used in gradient-based optimization are presented in Appendix A.

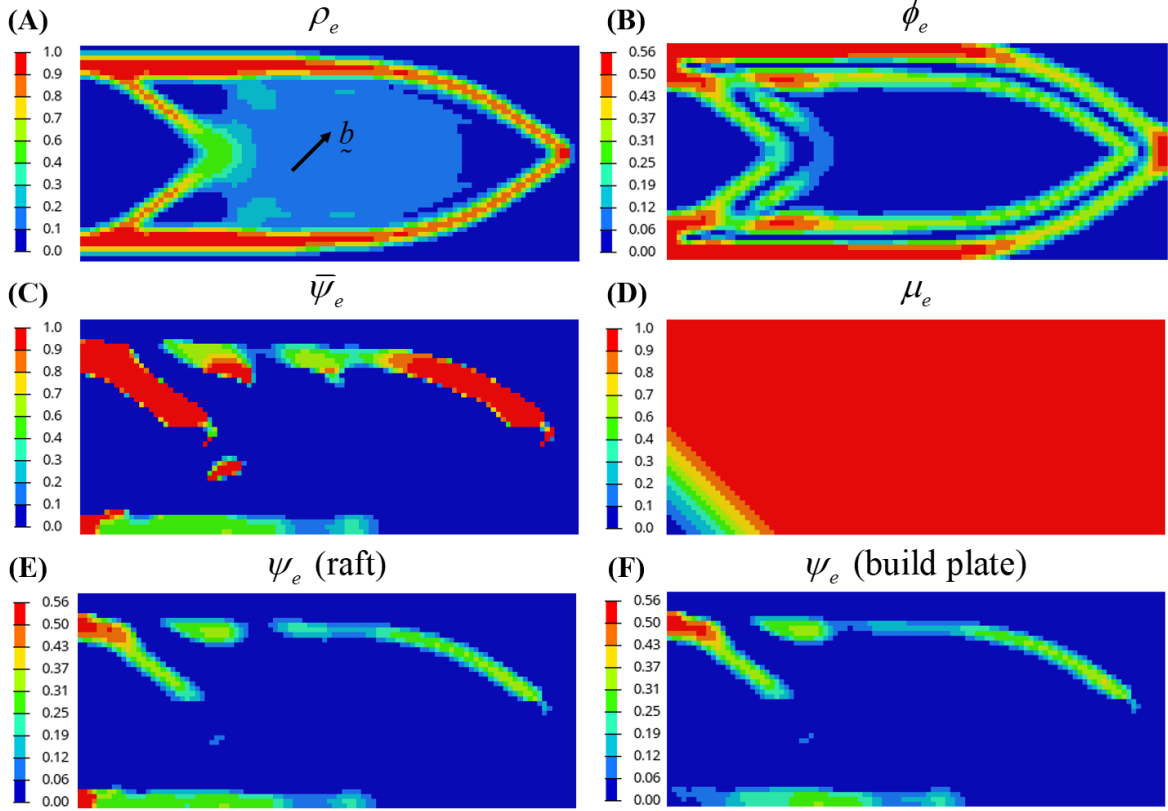


Figure 6 Demonstration of overhang area calculation for an intermediate 2D TO density field in (A) printed in the orientation indicated. The remaining plots show (B) surface area, (C) overhanging indicator, (D) build plate indicator, (E) overhang area when printed on a raft, and (F) overhang area when printed on the build plate.

## 2.5 Build Orientation Initialization

Build height and overhang area objective functions will have distinct local-minimum regions with respect to the build orientation design variables. This is illustrated in Figure 7 for a nearly converged TO solution, with build height and overhang area calculated over the complete build orientation design space in five-degree angle increments. While only  $\theta_2$  values between  $-90^\circ$  and  $90^\circ$  are needed to achieve all possible build orientations, these figures plot  $\theta_2$  over a  $360^\circ$  range for ease of visualization of the design space. For build height plotted in (B), a poor local minimum exists when  $\theta_l = 90^\circ$  (printing in the  $-x$  direction), where any small change in orientation would increase build height, but larger changes would drastically reduce height. While less evident, local minima exist in overhang area in (C), for example at  $\theta = (-115^\circ, 90^\circ)$  with a 43% increase in overhang area compared to the global optimum at  $\theta_l = 90^\circ$ . When printing on the build plate, overhang area in (D) has many local

minima at orientations where a flat face is closely aligned with the build plate, such as at  $\theta = (10^\circ, 90^\circ)$ ,  $\theta = (5^\circ, 0^\circ)$ , and when  $\theta_l = -90^\circ$ .

The selection of initial orientation vector is therefore crucial when using gradient-based optimization to avoid convergence to poor local minima. For simple problems, it may be possible to intuitively select an initial orientation, however this becomes more challenging for problems with complex geometries. Additionally, selecting an initial orientation is more difficult when AM cost metrics have conflicting behaviour with respect to orientation. For the example shown, there are distinct regions of the build orientation design space that result in low build height but large overhang area (such as  $\theta_l = 0^\circ$ ) and vice versa (at  $\theta_l = -90^\circ$  and  $\theta_l = 90^\circ$ ). This trade-off between height and overhang area occurs in many problems (such as the cantilever and MBB beam) and is unexplored in literature. For these problems, the ideal build orientation will depend on the desired weighting factor between AM-cost objectives.

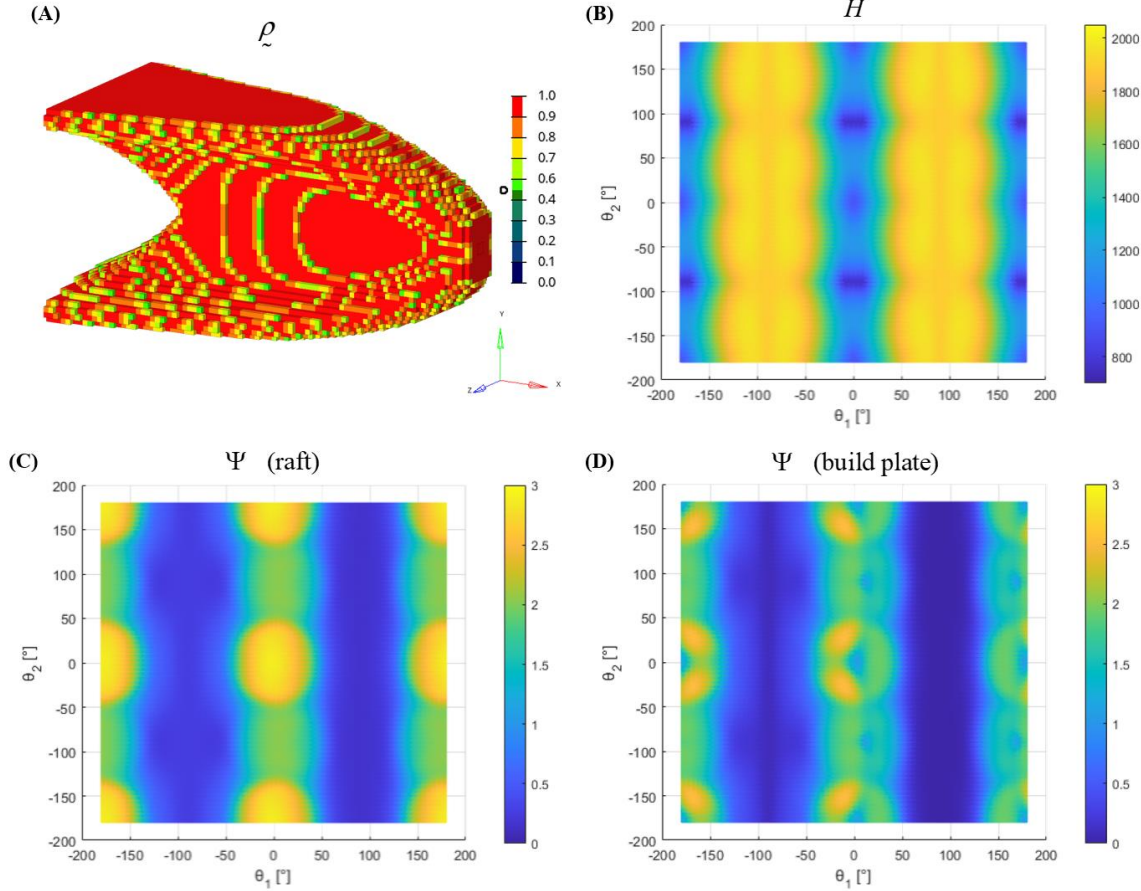


Figure 7 Plot of AM objective functions with respect to build orientation design variables for the TO result in (A). Build height is plotted in (B) and overhang area is plotted when printing on a raft in (C) and printing on the build plate in (D).

To achieve better solutions without needing to rerun the optimization with multiple initial orientation vectors, the automatic build orientation workflow described in Figure 8 is proposed. In this approach, the AM cost objectives are evaluated over a set of build orientation angles  $S_1 = \{\Delta, 2\Delta, \dots, 360^\circ\} - 180^\circ$  and  $S_2 = \{\Delta, 2\Delta, \dots, 180^\circ\} - 90^\circ$ , where  $\Delta$  is a large angle (such as  $\Delta = 45^\circ$ ) to search the design space in coarse intervals. The build orientation design variables are then initialized to the orientation vector  $(\theta_{m^*}, \theta_{n^*})$  that results in the lowest weighted sum of AM objectives. Rather than performing this orientation search at the start of the optimization, the optimization is run with only a compliance objective function for a set number of iterations  $i_\theta$  to achieve a preliminary density field without considering AM cost. With this approach, build orientation is initialized based on the preliminary topology rather than the input design space with uniform element densities. This can significantly change the selected orientation as some regions of the design space often quickly converge to low density values. AM cost cannot be considered before the orientation search as build height and overhang area are both functions of build orientation. The orientation search is followed by

gradient-based optimization of both the density and orientation design variables.

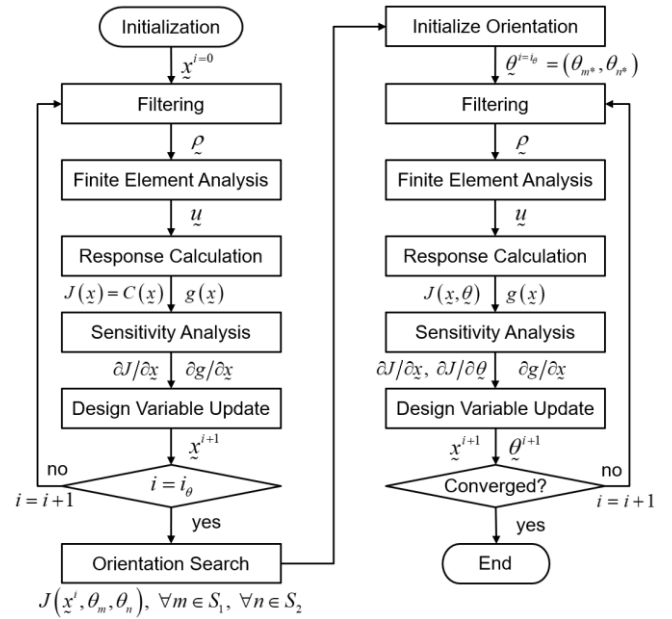


Figure 8 Flowchart describing the proposed automatic build orientation methodology where build orientation is initialized after a coarse search of the orientation design space with an early topology density field.

It is evident that the number of preliminary iterations completed without AM cost will have an impact on final topology and orientation of the structure. When performing the orientation search and subsequently beginning cost minimization, the density should ideally be:

- a) as close as possible to a uniform distribution to avoid poor local minima with respect to part topology; but also
- b) sufficiently defined to avoid poor local minima with respect to build orientation.

These are competing factors as the first favours an earlier orientation search, while the second favours a later orientation search. For the problems explored in this work, performing the orientation search as early as iteration 1 was able to find a favourable orientation. Beginning AM cost minimization at  $i_\theta = 5$  resulted in a less than 5% increase in final objective function values when compared to beginning AM cost minimization with uniform densities.

It should be noted that the proposed automatic orientation initialization approach is completely independent from the build height and overhang area optimization method also proposed in this work. The technique could be integrated into any other simultaneous topology and build orientation optimization approaches to avoid poor convergence behaviour with respect to build orientation. Likewise, the build height and overhang area optimization methodology can be performed without the automatic orientation initialization technique.

### 3 Numerical Methods and Results

The proposed topology and build orientation approach was implemented in a custom code using Altair OptiStruct for FE analysis and the Method of Moving Asymptotes (MMA) for gradient-based optimization (Svanberg 1987). A four-phase continuation scheme was used to improve convergence behaviour with the relevant parameters summarized in Table 1. The penalty factor and select smooth Heaviside slope parameters were increased as indicated after the change in objective function value was below 0.5% for the last two iterations. This continuation scheme starts the optimization with smooth approximations of overhang area and build height and approaches a more discrete calculation with the start of each new phase. The increase in penalty factor and density Heaviside slope help drive the optimization towards more discrete element density values. The interface radius was initialized at a large multiple of the

average element size and gradually decreased each phase to prevent the boundary oscillation or dripping effect (Garaigordobil et al. 2021). A self-supporting threshold of  $\bar{\alpha} = 45^\circ$  and a density filter radius of  $2.5 \times$  the average element size was used.

The final physical densities of the optimization were thresholded to 0-1 discrete values using a bi-section algorithm to remove any effects that intermediate densities have on the final design (Sigmund 2022). Objective function values were recalculated with modified smooth parameters to provide nearly discrete calculations of height and overhang area, so that the effectiveness of the optimization approach could be fairly evaluated. All figures show the thresholded physical density field and plot the final response fields calculated using the discrete parameter values. Figure 9 demonstrates the thresholding process for a sample topology optimization result. Note that this bi-section threshold and discrete calculation were not mandatory to achieve viable solutions and were included to ensure a fair comparison between results. Intermediate densities could be further reduced by adding more phases to the optimization with increased penalty factor and Heaviside slope parameters. However, this would increase computational time while yielding little difference in the final thresholded design.

Table 1 Summary of multi-phase continuation scheme used in optimization

	Phase 1	Phase 2	Phase 3	Phase 4	Discrete
$p$	2	3	4	5	-
$R_F$	2.5	2.5	2.5	2.5	-
$R_I$	5.5	4.5	3.5	2.5	1.5
$\alpha$	100	100	100	100	500
$\beta_\rho$	1	2	4	8	-
$\beta_\phi$	4	8	16	32	100
$\beta_\psi$	10	10	10	10	100
$\beta_\mu$	8	16	32	64	100
$\eta_\mu$	9	5	2	1	2.5
$\varepsilon$	0.01	0.01	0.01	0.01	0.001

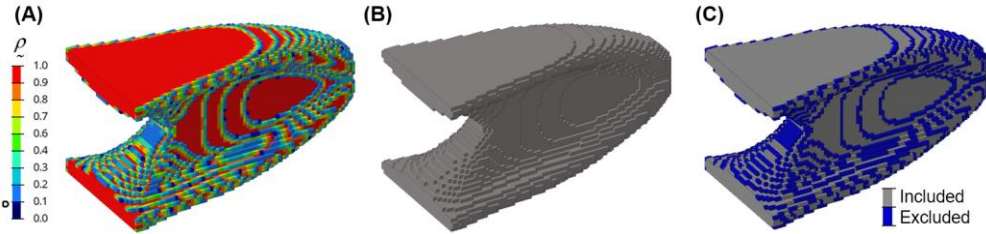


Figure 9 Comparison for a sample TO result of (A) final element densities with a 0.1 iso cut, (B) bi-section thresholded element densities, and (C) a 0.1 iso cut of final element densities indicating which elements were thresholded to 0 and 1 values.

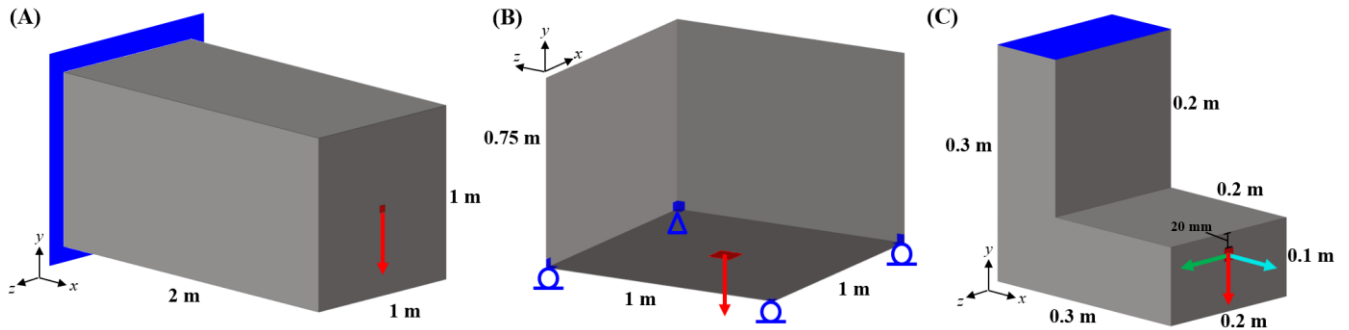


Figure 10 Academic test problems used for verification: (A) cantilever beam ( $80 \times 40 \times 40$ ) with  $C_{DS} = 0.364$  mJ, (B) simply supported box ( $60 \times 45 \times 60$ ) with  $C_{DS} = 1.042$  mJ, and (C) L-bracket ( $75 \times 75 \times 50$ ) with  $C_{DS} = 18.56$  mJ summed over all load cases.

The 3D academic test problems shown in Figure 10 were considered for numerical verification of the proposed methodology. A material stiffness of  $E_0 = 70$  GPa was used, and an applied load of 1000 N was evenly distributed over an area of  $50 \times 50$  mm in (A),  $100 \times 100$  mm in (B) and  $16 \times 16$  mm in (C). The compliance of the design space  $C_{DS}$  is listed in the figure description to aid with replication of results. The domain extension approach (Clausen and Andreassen 2017) was used with solid elements at loads and supports instead of local modifications as described by (Sabiston and Kim 2019), adding two layers of boundary elements around the exterior surfaces of the structure in addition to the element numbers listed (except for the constrained face of the cantilever beam and the L-bracket). This resulted in approximately 159k elements, 201k elements, and 199k elements, respectively. The cantilever beam problem was solved with a volume fraction of  $\bar{V} = 0.3$  while the box problem used a  $\bar{V} = 0.15$  constraint.

Element design variables were initialized at the volume fraction constraint and build orientation design variables were initialized as discussed in each section. Objective function values were normalized to ensure similar values during optimization. Compliance was normalized based on the compliance of the initial iteration  $C_0 = C(\underline{x} = \bar{V})$ , overhang area was normalized based on the total surface area of the design space  $\Psi_0 = \sum_{e \in N} \phi_e(\rho = 1)$ , and build height was normalized using the average build height of the design

space in the three principal directions  $H_0 = \sum_{\theta \in S} H(\rho = 1, \theta) / 3$  where  $S = \{(0^\circ, 0^\circ), (90^\circ, 0^\circ), (0^\circ, 90^\circ)\}$ . The orientation-dependent objectives were normalized without reference to orientation to ensure the weighting factor magnitudes did not depend on the selected initial orientation.

### 3.1 Build Height Topology Optimization

Simultaneous compliance and build height minimization for a fixed orientation was illustrated by setting the  $w_2$  weighting factor equal to 1 and varying the  $w_1$  weighting factor between 0.3 and 1. A Pareto frontier for the cantilever beam problem with a fixed print orientation in the  $z$  direction is shown in Figure 11, with compliance and height values normalized relative to the purely structural solution. In this orientation, the  $w_1 = 0.9$  result provides a reasonable trade-off between objectives with a 6% increase in compliance resulting in a 41% reduction in build height. As the structural weighting factor decreases, the component is gradually flattened with further increases in compliance.

When printing in a less favourable orientation as shown in Figure 12, a reduction in height is more expensive, with the  $w_1 = 0.3$  solution resulting in a 46% reduction in height and a 138% increase in compliance. The significantly worse compliance is expected as the bending area moment of inertia is much more sensitive to the height of the cantilevered beam

(in the direction aligned with the load) compared to its base. Another observation from this example is that the weighting factor change from  $w_1 = 1.0$  to  $w_1 = 0.7$  had an almost negligible impact on the height of the component. This occurred because the optimization is minimizing a smooth approximation of height rather than the true height of the

component. From a fully discrete height calculation, the  $w_1 = 1.0$  component would have the same height as the  $w_1 = 0.7$  solution, however the later component has only a few elements contributing to this height that could be removed during design interpretation.

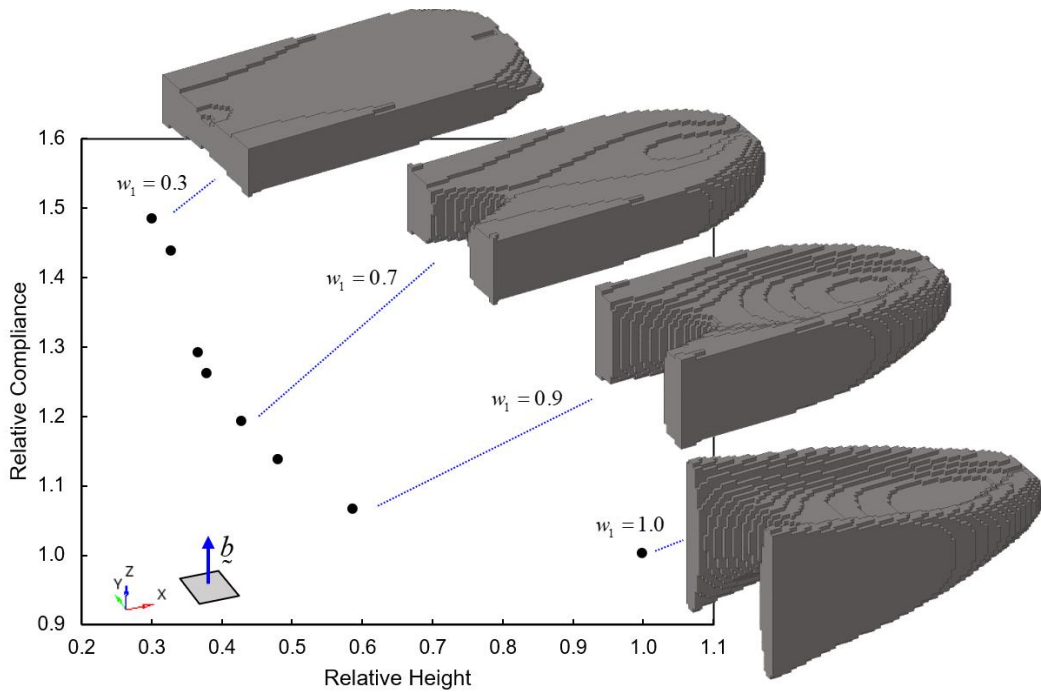


Figure 11 Pareto frontier of relative compliance and height for the cantilever beam problem at a fixed orientation of  $\theta = (0^\circ, 90^\circ)$ .

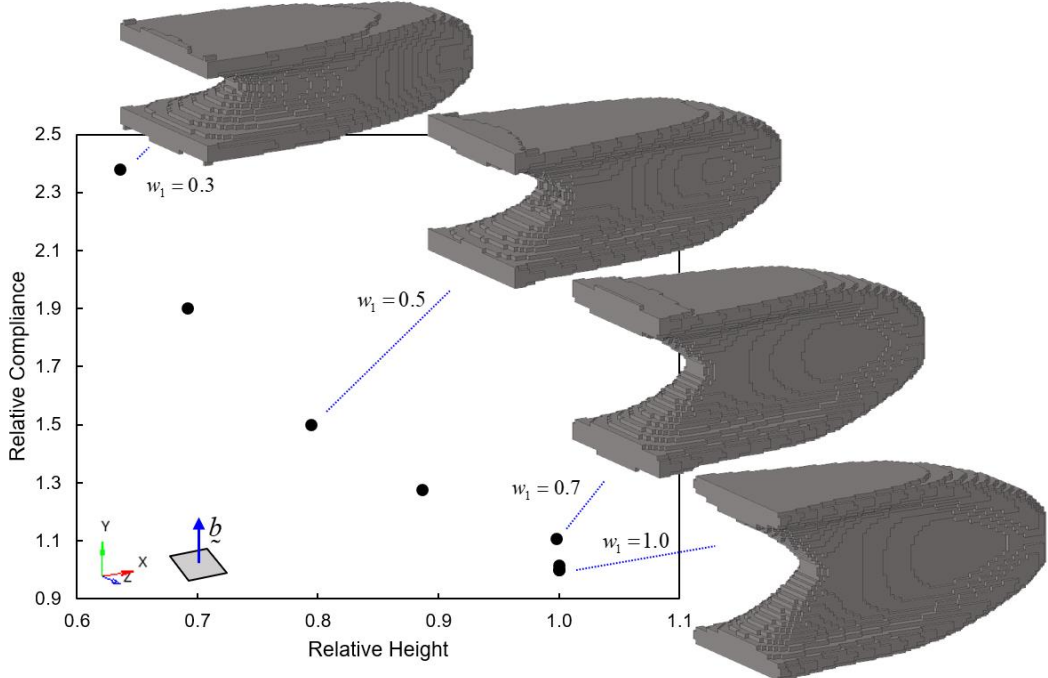


Figure 12 Pareto frontier of relative compliance and height for the cantilever beam problem at a fixed orientation of  $\theta = (0^\circ, 0^\circ)$

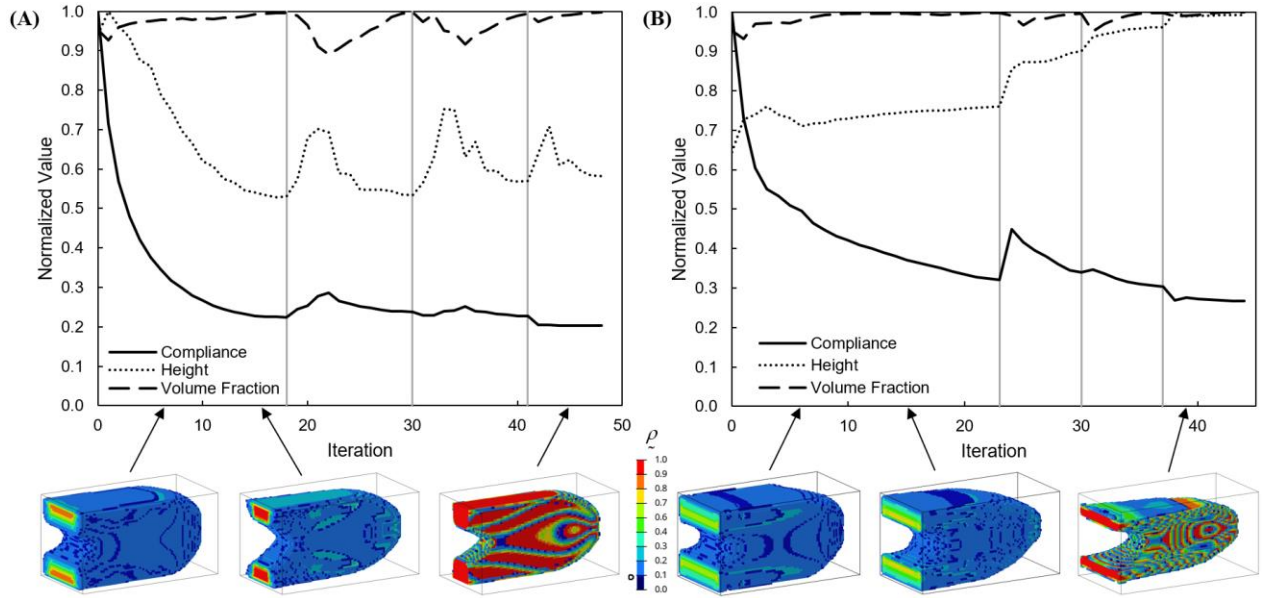


Figure 13 Convergence plots of normalized compliance, height, and volume fraction for (A) the  $w_i = 0.7$  result from Figure 11, and (B) the  $w_i = 0.5$  result from Figure 12. Optimization phases are indicated by vertical grey lines and element density contour plots are included at select iterations with an iso cut value of 0.1.

Plots of objective and constraint function history are displayed in Figure 13 for two build height optimization runs. Objective values are normalized relative to the maximum value throughout the optimization, while constraint values are normalized relative to the constraint limit. Convergence history shows smooth behaviour with abrupt changes at the start of each new phase. The build height objective increased throughout the optimization because distance terms are scaled in Equation (13) by physical densities, which have intermediate values at the start of the optimization and gradually converge to discrete 0-1 values.

The effect of the  $\alpha$  smooth minimum and maximum parameter on the optimization is highlighted in Figure 14. To visualize the reduction in height throughout the optimization, the exact height was calculated at each iteration using discretely thresholded densities (with a  $\rho = 0.3$  cutoff). For very low values of  $\alpha$ , the resultant designs have angled top and bottom surfaces, indicating that the height calculation is too smooth. On the other hand, with a very large  $\alpha$  value, the height calculation is too discrete, and the optimizer is not able to effectively minimize height due to oscillating convergence behaviour. While the  $\alpha=100$  result in (D) most effectively minimizes height, the top and bottom surfaces of the component are slightly angled as this height calculation is a smooth function. It should be noted that the smoothness of the maximum function in Equation (16) scales with both the  $\alpha$  value and the dimensions of the model. To ensure that the same  $\alpha$  parameter can be used for any input geometry, the current implementation automatically scales

element height values between zero and one before starting the optimization.

It is evident from this example that some orientations are more favourable for height minimization, and it should also be acknowledged that for this example, minimizing height in the  $x$  direction would not be possible as there are constraints and loads at the extremities of the design that dictate the component height in that direction.

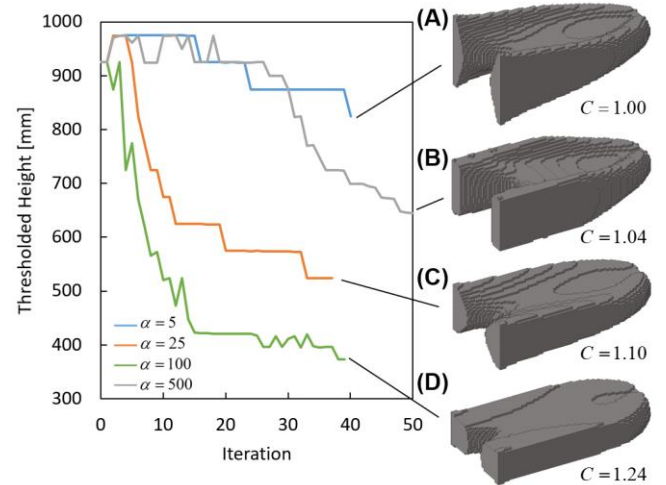


Figure 14 Effect of smooth maximum and minimum parameter  $\alpha$  on height minimization. All optimizations used a weighting factor of  $w_i = 0.6$  and compliance values area normalized relative to (A).

### 3.2 Overhang Area Topology Optimization

Overhang area and compliance minimization was demonstrated by setting the  $w_2$  weighting factor equal to 0

and varying the  $w_1$  weighting factor between 0.5 and 1. This set of optimization runs was completed with both the raft option (setting  $\mu=1$  for all elements) and the build plate option (calculating  $\mu$  as described). Figure 15 shows a Pareto frontier for the raft and build plate option when printing in a fixed orientation of  $\theta=(0^\circ, 0^\circ)$ . Components are plotted with a contour of overhanging area, with non-overhanging elements plotted in gray. Objective function values were normalized relative to the baseline  $w_1=1$  solution for each set of results. When printing on the build plate, a 97% reduction in overhang area was achieved with a 3% increase in compliance in the  $w_1=0.5$  solution. In addition to this nearly overhang-free result, this approach can also provide a range of solutions, such as the  $w_1=0.9$  result that reduces overhang area by 59% with very minor changes to the geometry and a 0.4% increase in compliance. When building on a raft, which cannot be considered with self-supporting approaches in literature, the entire bottom surface is considered overhanging, making it more difficult to reduce overhang area. The  $w_1=0.5$  solution reduces overhang area by 72% with a 7% increase in compliance.

These optimizations were also completed for the fixed orientation of  $\theta=(0^\circ, 90^\circ)$ , with results summarized in Figure 16. Note that the components are not oriented in their print direction in this figure for easier visualisation. This build orientation is a more challenging orientation for overhang area minimization as the baseline cantilever design has a large overhanging surface. Conventional self-supporting optimization approaches from literature would

make significant changes to this geometry to build upwards from the bottom of the design space. Instead, when printing on the build plate, the optimizer aligns the bottom of the component to a single plane, effectively raising the build plate to reduce overhang area by 99% with an 8% increase in compliance. A very different solution is obtained when printing on a raft, which achieved an 85% reduction in overhang area with the same increase in compliance, as there is no incentive for the optimizer to align the bottom of the component to a single plane. In this case, the optimizer reduces the overhanging surface to an overhanging edge with one element thickness. When printing on a raft, it is impossible to remove all overhanging surfaces, as even in the most extreme case, the component must build upwards from at least one element. As the  $w_1$  weighting factor is reduced, overhanging surfaces at the bottom of the component will gradually shift towards an overhanging edge and icicle structures will eventually form to further reduce overhanging area. These icicle structures are present in the  $w_1=0.6$  raft solution and are circled in Figure 16. While the icicle structures are often described as undesirable in the final design, they are a feasible technique to reduce overhang area when printing on a raft, especially after the design has converged to build from a single overhanging edge. In the approach proposed in this work, icicle structures are avoided in most cases through the interface radius continuation scheme, and in cases where icicles are present, the weighting factor on overhang area can be reduced to avoid these features. Weighting factors below  $w_1=0.6$  produced poor results with several icicle structures for this orientation when printing on a raft.

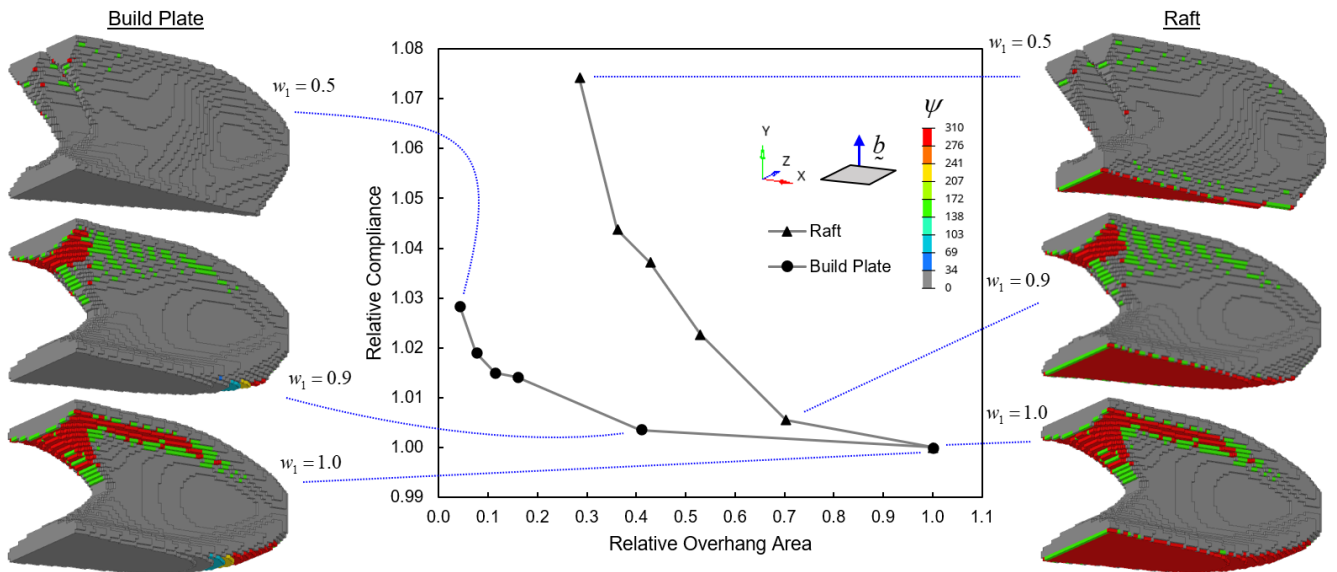


Figure 15 Pareto frontier of relative compliance and overhang area when building on a raft and build plate for the cantilever beam problem at a fixed orientation of  $\theta=(0^\circ, 0^\circ)$ . Objective function values are normalized relative to the respective  $w_1=1.0$  result.

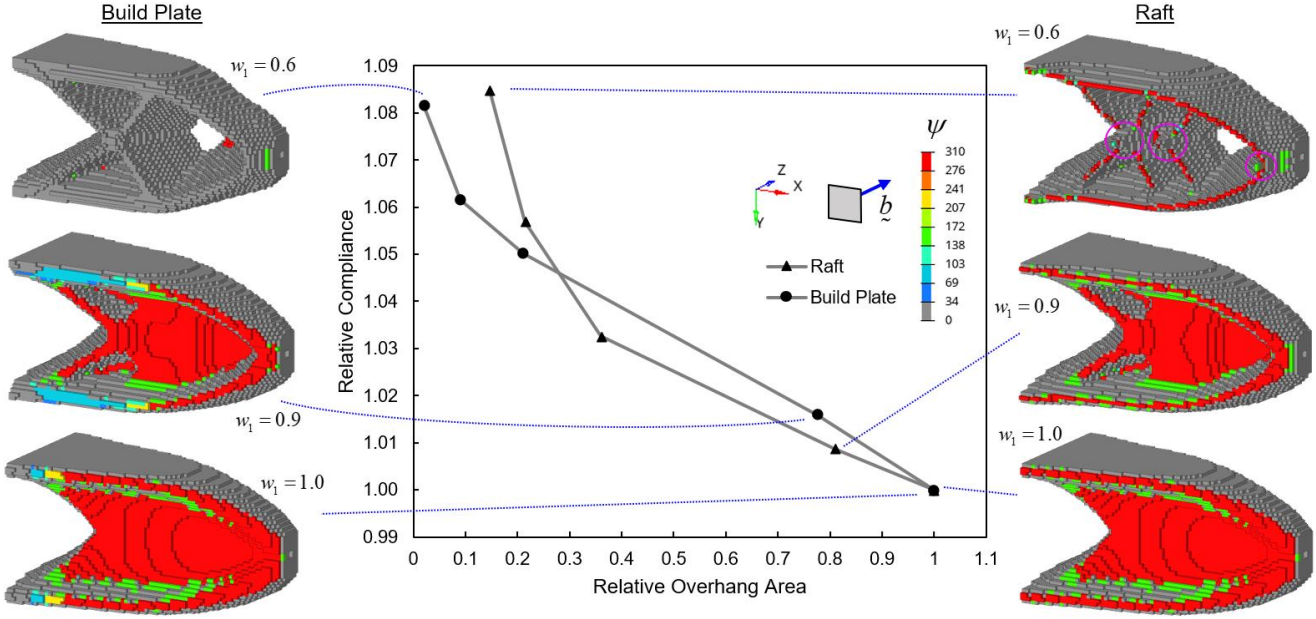


Figure 16 Pareto frontier of relative compliance and overhang area when building on a raft and build plate for the cantilever beam problem at a fixed orientation of  $\theta = (0^\circ, 90^\circ)$ . Objective function values are normalized relative to the respective  $w_1 = 1.0$  result. Icicle structures are circled in the  $w_1 = 0.6$  raft solution.

Objective and constraint function history in Figure 17 for overhang area minimization shows smooth behavior. Significant changes occur at the start of each phase, where penalty function and Heaviside threshold slopes are increased. The overhang area objective function gradually increased throughout the optimization when printing on the build plate in (B) because the initial design had no

overhanging area. As the preliminary structure formed, overhanging surfaces began to emerge and the build plate identifier field began to identify the base of the part. As the densities became more discrete in phases 3 and 4, the optimization successfully eliminated nearly all overhanging surfaces.

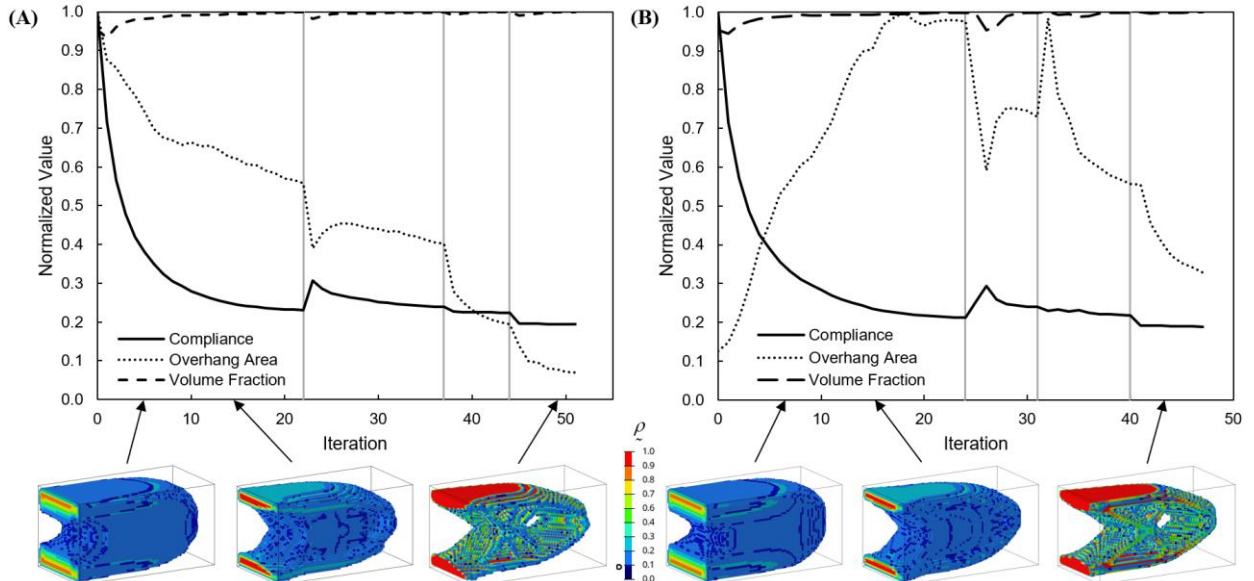


Figure 17 Convergence plots of normalized compliance, overhang area, and volume fraction for the  $w_1 = 0.6$  result from Figure 16 when printing on (A) a raft and (B) the build plate. Optimization phases are indicated by vertical grey lines and contour plots are included at select iterations with an iso cut value of 0.1.

The differences in component geometry between printing on the build plate compared to a raft are highlighted in Figure 18. When printing in the  $y$  direction, the raft solution in (B) has a significantly reduced bottom overhanging surface and builds the component upwards from this reduced area, while the build plate solution in (A) has a large bottom surface on the build plate to increase the bending area moment of inertia. When printing in the  $z$  direction, the build plate solution in (C) has a flat bottom surface to raise the build plate, while the raft solution in (D) has a single overhanging edge with varying element height. Note that neither of these solutions are required to print directly from the bottom of the design space, which is enforced in self-supporting optimization algorithms in literature.

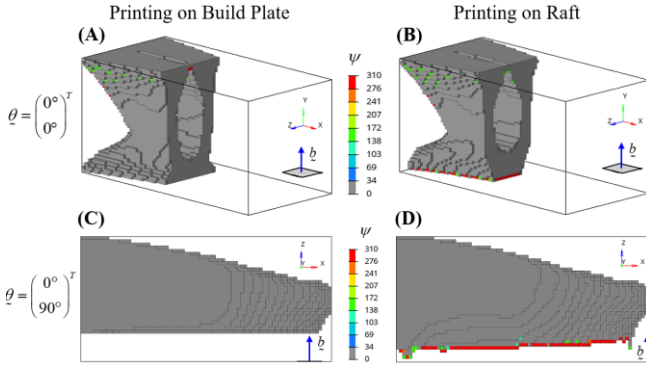


Figure 18 Comparison showing the influence of building on the build plate compared to building on a raft when a large weighting is placed on overhanging area ( $w_1 = 0.6$ ).

The proposed overhang area minimization method was compared to other approaches in literature in Appendix B, showing similar performance in most cases and all results within 10% of reported performance metrics.

### 3.3 Topology and Build Orientation Optimization

The optimization problem was extended by adding the build orientation design variable to conduct simultaneous topology and build orientation optimization. Figure 19 shows the build height and overhang area optimization (considered separately), starting from the four initial build orientation angles indicated as well as with the automatic build orientation initialization approach. Components are oriented in their respective print orientation with the build plate plane depicted in grey. All optimizations used a weighting factor of  $w_1 = 0.8$  and objective function values are normalized across each row. With the build height (A1-A4) and overhang area with build plate (C1-C4) objectives, the optimization converged to a different local minimum orientation for each  $\theta^{init}$  value. The overhang area with raft (B1-B4) converged to a similar orientation with three of the initializations due to a smoother objective function with fewer local minimum

orientations. In all cases, the automatic orientation initialization scheme converged to the best orientation achieved from the four manual initializations. With respect to the selected AM objective function, the automatic initialization achieved an 8% better solution in (A5), a 4% worse solution in (B5), and an equivalent solution in (C5). For this cantilever beam problem, the computational cost of the orientation search was approximately equivalent to one FE analysis operation, which is negligible over the course of the optimization process. Convergence history for simultaneous topology and build orientation results (B1) and (B5) is included in Appendix C.

Rather than referring to the final orientation design variable values when determining if two results converged to a similar orientation, the depicted component orientations should instead be referenced. For example, in (B3) and (C3) (where  $\theta_1 = 90^\circ$ ), the  $\theta_2$  rotation does not change the build orientation as the build direction vector is aligned with the  $x$  axis. The symmetry of the cantilever beam problem can also cause two different build orientation angles to result in the same effective orientation, such as in (B1) and (B4).

Another important point of discussion is that in (B2) and (C2), the build orientation design variables converged to values outside the angle limits specified in the problem statement in Equation (1). These limits were defined based on the smallest possible range of orientation design variables needed to achieve any build direction vector, when realistically, any orientation design variable value is valid as the cosine and sine functions used in the rotation calculation in (10) are periodic. In this implementation, the MMA upper and lower design variable bounds for the orientation design variables were set to artificially high and low values to prevent the orientation angles from getting caught in a local minimum at an artificial design variable bound. The resultant orientation design variables can be translated to an equivalent feasible orientation angle, denoted in Figure 19 with an asterisk.

The iteration  $i_\theta$  at which build orientation initialization is performed influences the effectiveness of the automatic initialization approach, as demonstrated in Figure 20 for build height optimization. If the orientation search is performed too early in the optimization, such as at iteration 0 in (A), the geometry may not be sufficiently well-defined to identify the best starting orientation. On the other hand, when performing this search too late in the optimization, such as at iteration 20 in (C), the geometry will be too well-defined for the optimizer to effectively minimize the AM objective, resulting in a 17% increase in height relative to design (B). While not pictured in Figure 20, orientation initialization at iterations 1 and 10 resulted in the same orientation as (B)-(C) and achieved within 5% of the build height of (B).

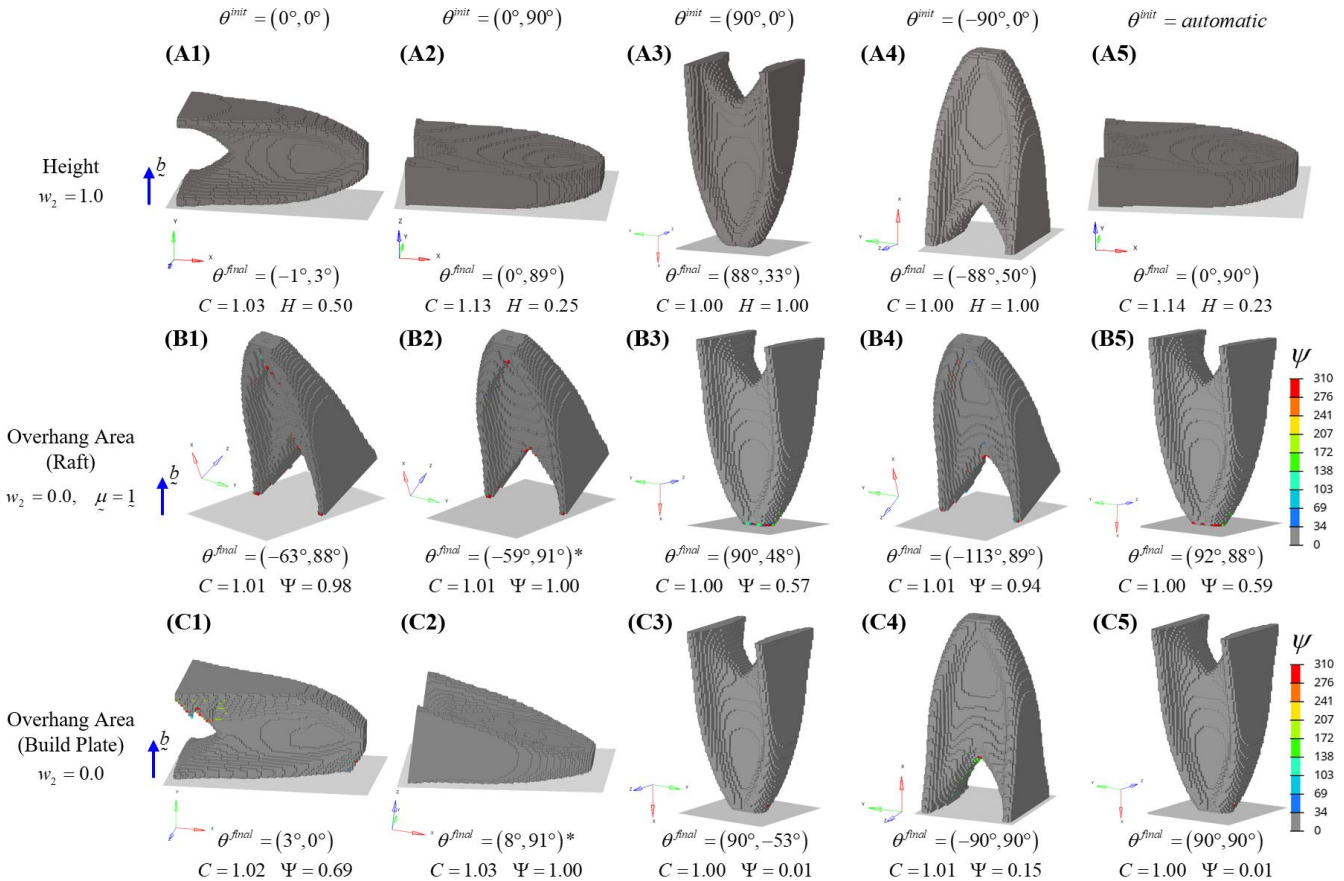


Figure 19 Simultaneous topology and build orientation optimization comparing four build orientation angle initializations and the proposed automatic build orientation initialization method. (A1-A5) considers build height, (B1-B5) considers overhang area printing on a raft, and (C1-C5) considers overhang area printing on the build plate.

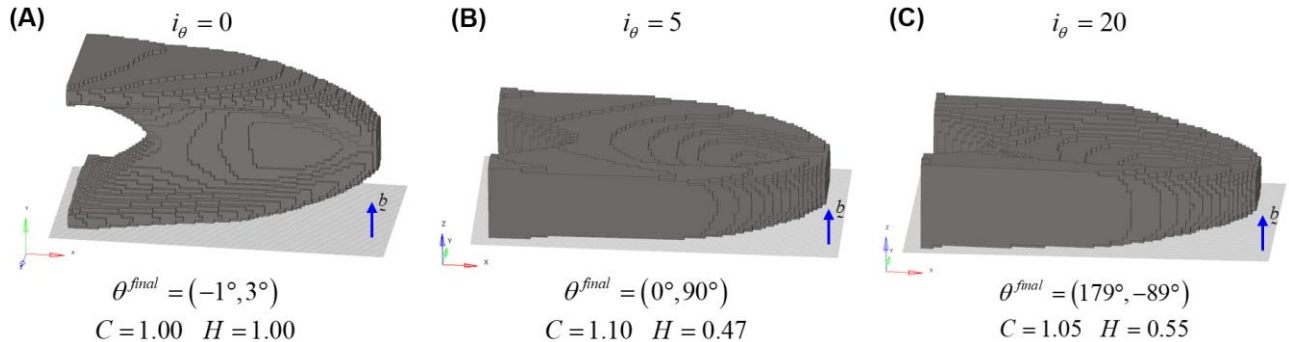


Figure 20 Influence of selected iteration for automatic build orientation initialization when optimizing for build height. All optimizations used weighting factors of  $w_1 = 0.8$  and  $w_2 = 1.0$ .

The step size  $\Delta$  used for the set of search angles also has an impact on the effectiveness of the orientation search to identify the ideal orientation, and the computational time of the approach. For simple convex design spaces, the step size of  $\Delta = 45^\circ$  is expected to be sufficient to achieve an effective orientation, however smaller search angles may be needed as geometric complexity is increased. Preliminary testing has shown a step size of  $\Delta = 20^\circ$  to be equivalent to 3 – 4 FE analyses, while a step size of  $\Delta = 5^\circ$  was equivalent to an

increase in the total optimization computational time by 20 – 40%, which is a significant time savings when compared to rerunning the optimization with multiple initial orientation vectors.

### 3.4 Multi-Objective Topology and Build Orientation Optimization

Build height and overhang area were considered simultaneously during topology and build orientation

optimization for the cantilever beam problem by varying the  $w_2$  weighting factor in 0.1 increments between 0 and 1, for two  $w_1$  weighting factor values. The results of this parameter sweep are plotted in terms of relative overhang area and relative build height in Figure 21 when printing on a raft. Select optimization results are plotted in their print orientation, alongside a contour plot of overhanging area from a bottom view in the dashed box. With a small weighting factor on AM objectives ( $w_1 = 0.99$ ), the optimizer essentially determines the topology based only on compliance, while the orientation is determined based on the desired trade-off between overhang area and height. Therefore all  $w_1 = 0.99$  results have nearly identical geometry and achieve the same compliance values but have different orientations to minimize the selected AM objective. For example, the orientation in result (A1) reduces overhang area by 94% relative to (A3) with an 108% increase in build height. The orientation in (A2) provides an intermediate trade-off between the height and orientation objectives. The  $w_1 = 0.99$  optimization produced clusters of results with nearly identical geometry and orientation at points (A1) and (A3), respectively.

The  $w_1 = 0.9$  optimization placed a lower weighting on compliance, resulting in the optimizer sacrificing structural

performance to reduce AM objectives. At  $w_2 = 0.0$ , the resultant component and orientation are essentially identical to (A1), as this orientation effectively eliminates overhang area without any modifications to the baseline structure. As the  $w_2$  weighting factor is increased, the optimization shifts towards minimizing build height, and compliance gradually increases. For example, result (A4) achieved an 11% reduction in overhang area and a 21% reduction in build height relative to (A3), with an associated 3% increase in compliance. At  $w_2 = 1.0$ , the optimization focused entirely on build height, resulting in a 38% reduction in height relative to (A3), accompanied by a 21% increase in overhang area and a 7% increase in compliance.

These results show a clear trade-off between the build height and overhang area when moving along a line of constant  $w_1$  weighting factor. When moving between lines of constant  $w_1$ , it is possible to achieve a reduction in both AM objectives, albeit with an increase in compliance. It is therefore important to identify the importance of each AM objective function for the selected AM method and to consider them accordingly when optimizing the geometry and print orientation of a component.

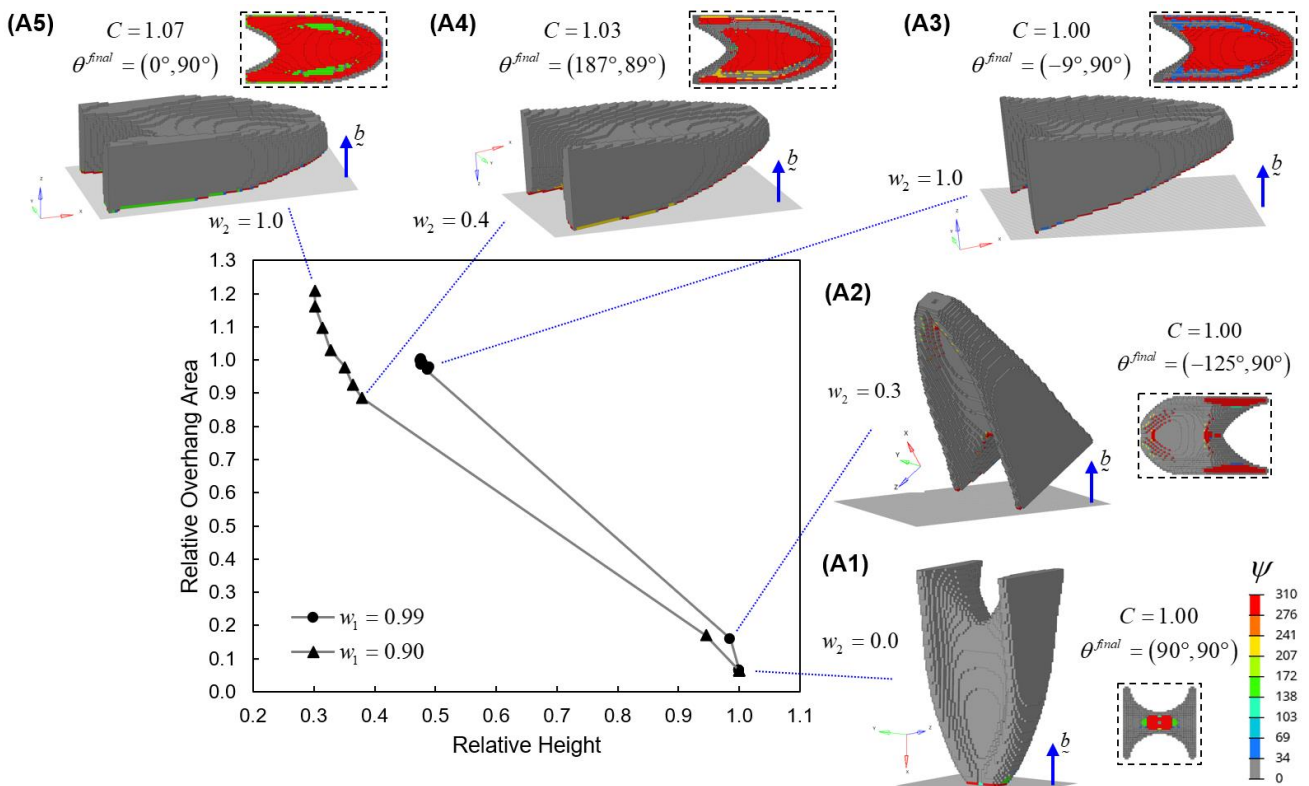


Figure 21 Plot of relative overhang area and height for the cantilever beam problem when printing on a raft solved with a range of weighting factors.

Figure 22 shows the same optimization process carried out for the cantilever beam when printing on the build plate. The  $w_1 = 0.99$  optimization converged to similar orientations from Figure 21 when considering only overhang in (B1) and only height in (B3). However, when building on a raft, the orientation shown in (B2) achieved the same height as (B3), but with a 28% reduction in overhang area because the bottom face of the cantilever beam is aligned with the build plate. By incorporating a small weighting on overhang area into the objective function, the optimizer was able to achieve an overall superior orientation that, when considering only height, was one of two equivalent orientations. With a larger weighting factor on AM objectives ( $w_1 = 0.9$ ), the optimization converged to a similar orientation as (B2) for weighting factors between  $w_2 = 0.2$  and 0.9. The typical Pareto frontier behaviour is not seen between results (B4) and (B5) because the third objective, compliance, is increasing as  $w_2$  increases. In this case, the optimizer achieved simultaneous reductions in overhang area and build height up to result (B5), after which the overhang area and compliance both increase as height is reduced. When printing on the build plate, both the build height and overhang area objectives favour designs with flat bottom surfaces, enabling the optimizer to generate designs that simultaneously reduce both objectives.

The same optimization process was carried out for the simply supported box model, with Figure 23 showing the results when building on a raft. The  $w_1 = 0.99$  results, which have similar geometry, converge to three different

orientations shown in (C1), (C2), and (C3). Each orientation results in a different trade-off between compliance and height with (C1) yielding a 69% reduction in overhang area and (C3) yielding a 48% reduction in height, relative to each other. A cluster of results is seen around result (C3) for weighting factors of  $w_2 \geq 0.2$ , which all converge to a similar orientation. Unlike the cantilever beam problem, the  $w_1 = 0.9$  optimizations were able to achieve further reductions in overhang area through small modifications to the geometry and orientation. For example, design (C5) achieved a 58% reduction in overhang area relative to (C2) at the same build height, with a 1% increase in compliance. Results (C4) through (C6) each converge to different orientations that gradually shift from favouring overhang area to build height. Weighting factors of  $w_2 \geq 0.3$  converge to the orientation shown in (C7), which is most favourable for build height reduction. Design (C7) produced a strong trade-off between AM objectives achieving a 57% reduction in build height and a 59% reduction in overhang area relative to designs (C1) and (C3), respectively, with a 3% increase in compliance. As with the cantilever beam problem, the compliance gradually increases with increasing  $w_2$  along the  $w_1 = 0.9$  line, as build height reduction is associated with a larger increase in compliance compared to overhang area. The only exception to this was the  $w_2 = 0.6$ , which achieved a lower compliance than the  $w_2 = 0.4$  and  $w_2 = 0.5$  results, meaning it is still a Pareto optimal solution when considering all three optimization objectives.

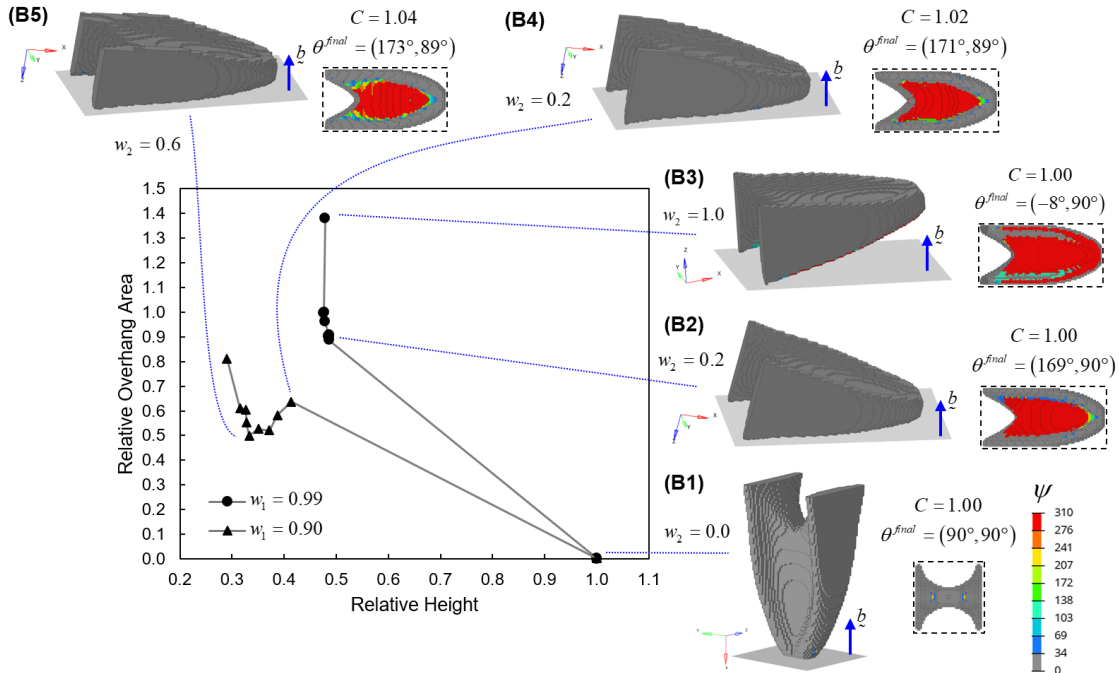


Figure 22 Plot of relative overhang area and height for the cantilever beam problem when printing on the build plate solved with a range of weighting factors.

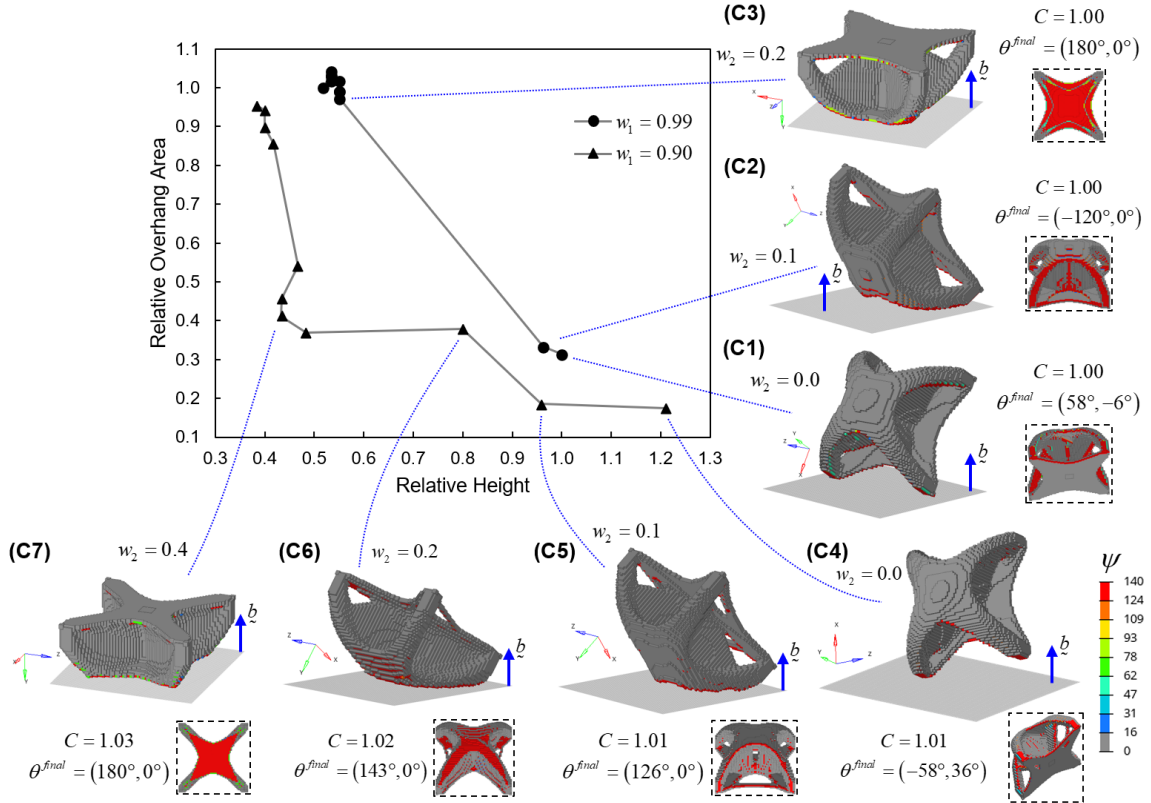


Figure 23 Plot of relative overhang area and height for the simply support box problem when printing on a raft solved with a range of weighting factors.

When solving the simply supported box problem for printing on the build plate, the  $\theta = (0^\circ, 0^\circ)$  orientation always results in the best trade-off between build height and overhang area. Therefore, all optimizations in Figure 24 converge to this orientation, except for (D5), which achieves the opposite printing orientation with an equivalent build height, but worse overhang area. This is the second example from the multi-objective optimization (in addition to (B2) from Figure 22) where a very small weighting on overhang area can help achieve an overall better orientation for both AM objectives. Result (D3) reduces overhang area by 82% relative to (D1) with the same build height and a 1% increase in compliance. For a strong trade-off between objectives, (D4) reduces height by 32% and overhang area by 56% relative to designs (D1) and (D2), respectively, with a 3% increase in compliance. Another important observation is that all results from Figure 24 achieve very different orientations and geometries when printing on the build plate compared to results achieved in Figure 23 when printing on a raft, highlighting the importance of considering this distinction during optimization.

### 3.6 Stiffness Constrained Optimization

The L-bracket problem from Figure 10 (C) was solved with a modified version of the original problem statement to

minimize the multi-objective sum of volume  $V$  and AM cost metrics subject to a set of  $M$  displacement constraints. The alternative problem statement is outlined in Equation (26), where  $u_i$  is the  $i$ -th displacement for a given node and degree of freedom and  $\bar{u}_i$  is the corresponding constraint limit. The volume is normalized by the volume of the initial iteration  $V_0$  and element densities were initialized to a value of  $x_0 = 0.9$ . The same four-phase convergence was used as outlined in Table 1, except for the filter radius of  $1.5 \times$  the average element size and an interface radius of  $4.5 \times$  decreasing by one each phase. Three displacement constraints were specified with values of  $\bar{u}_1 = 0.02$  mm,  $\bar{u}_2 = 0.06$  mm, and  $\bar{u}_3 = 0.05$  mm in the x, y, and z load cases, respectively.

$$\begin{aligned} \min J(\underline{x}, \theta) &= w_1 \frac{V(\underline{x})}{V_0} + (1-w_1) \left( w_2 \frac{H(\underline{x}, \theta)}{H_0} + (1-w_2) \frac{\Psi(\underline{x}, \theta)}{\Psi_0} \right) \\ \text{s.t. } & \underline{K}\underline{u} = \underline{f} \\ & g(\underline{x}) = u_i(\underline{x}) \leq \bar{u}_i, \quad i = 1, \dots, M \\ & 0 \leq x_e \leq 1, \quad e = 1, \dots, N \\ & -180^\circ < \theta_1 \leq 180^\circ \\ & -90^\circ < \theta_2 \leq 90^\circ \end{aligned} \quad (26)$$

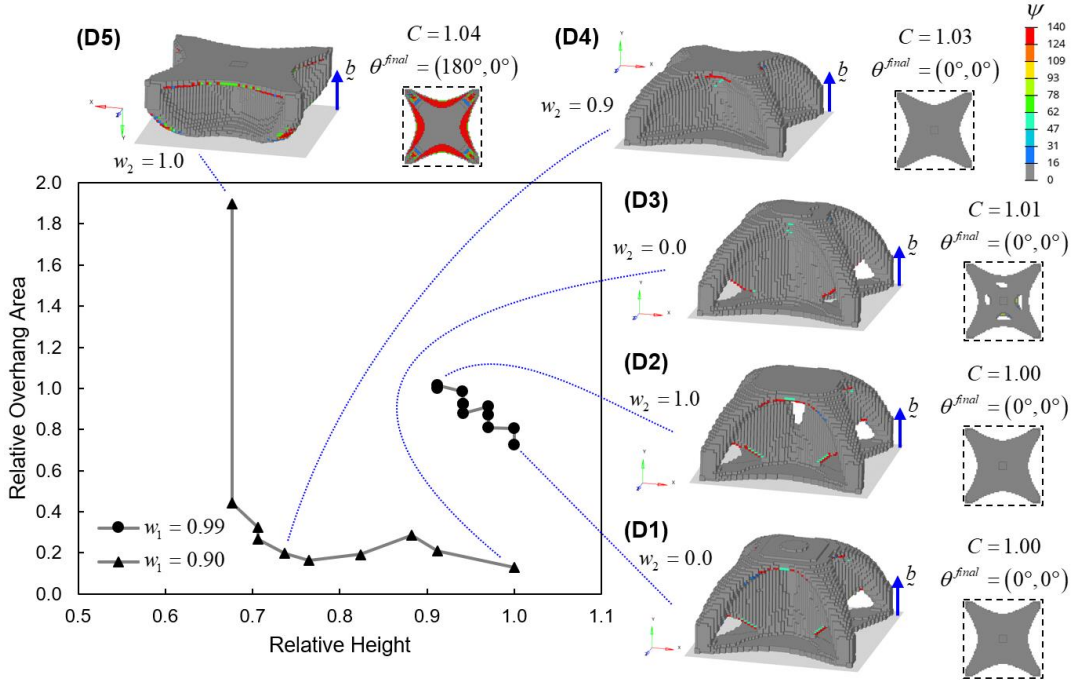


Figure 24 Plot of relative overhang area and height for the simply supported box problem when printing on the build plate solved with a range of weighting factors.

The baseline TO result with  $w_1 = 1$  in Figure 25 shows a complex geometry with a hollow interior and many internal stiffening members. This structure has significant overhanging surfaces in each orientation and presents a good challenge for the proposed approach. All results in this section are visualised with a smooth iso-filter of thresholded element density with a 0.4 iso cut value.

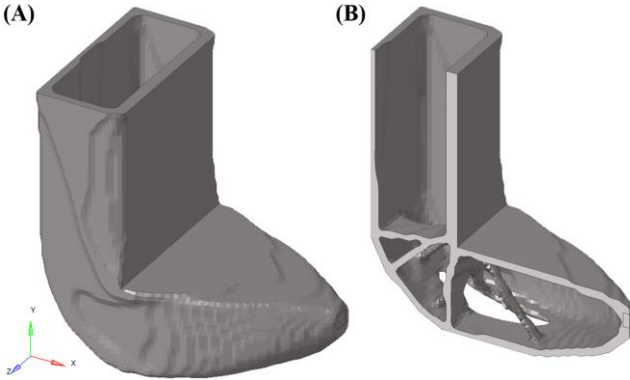


Figure 25 Baseline TO results for stiffness constrained L-bracket problem with (B) showing a cross-section about the mid-plane.

The stiffness constrained problem statement in Equation (26) was optimized for  $w_2$  weighting factors from 0 to 1 in 0.2 increments over two  $w_1$  weighting factors using automatic build orientation initialization. Select results are displayed in Figure 26 in the final build orientation with a

cross-section view indicating the internal overhanging surfaces. The top row of results with  $w_1 = 0.99$  demonstrates a clear trade-off between overhang area and build height. The orientation in (E3) had a 52% reduction in height but a 3× increase in overhang area when the L-bracket was built on its side compared to the orientation in (E1). With a larger weighting on AM cost, design (E4) reduced overhang area by 73% for the same orientation as design (E1) with a 3% increase in volume. Design (E5) achieved a 64% reduction in overhang area relative to (E3) and a 49% reduction in height relative to (E1), but with a 13% increase in volume. As with the previously explored problems, these results show that the proposed approach can effectively minimize both build height and overhang area, however the more complex geometry of the L-bracket problem resulted in a larger performance reduction when minimizing both AM cost metrics. Convergence history for multi-objective, stiffness-constrained topology and build orientation optimization result (E5) is included in Appendix C.

### 3.5 Slicer Verification

To verify that the reduction in AM cost driving metrics calculated during optimization were translated to real-world AM cost reduction, select results from Figure 21 – Figure 26 were verified using a slicer software for a FDM printer. An iso filter with a value of 0.5 was taken of the final physical density field using a simple average in Altair HyperView.

The exported .STL file was smoothed using Autodesk Meshmixer “smooth” tool and imported into PrusaSlicer v2.5.0 and sliced using the settings outlined in Appendix D.

This process is depicted visually in Figure 27 for a sample simply supported box result.

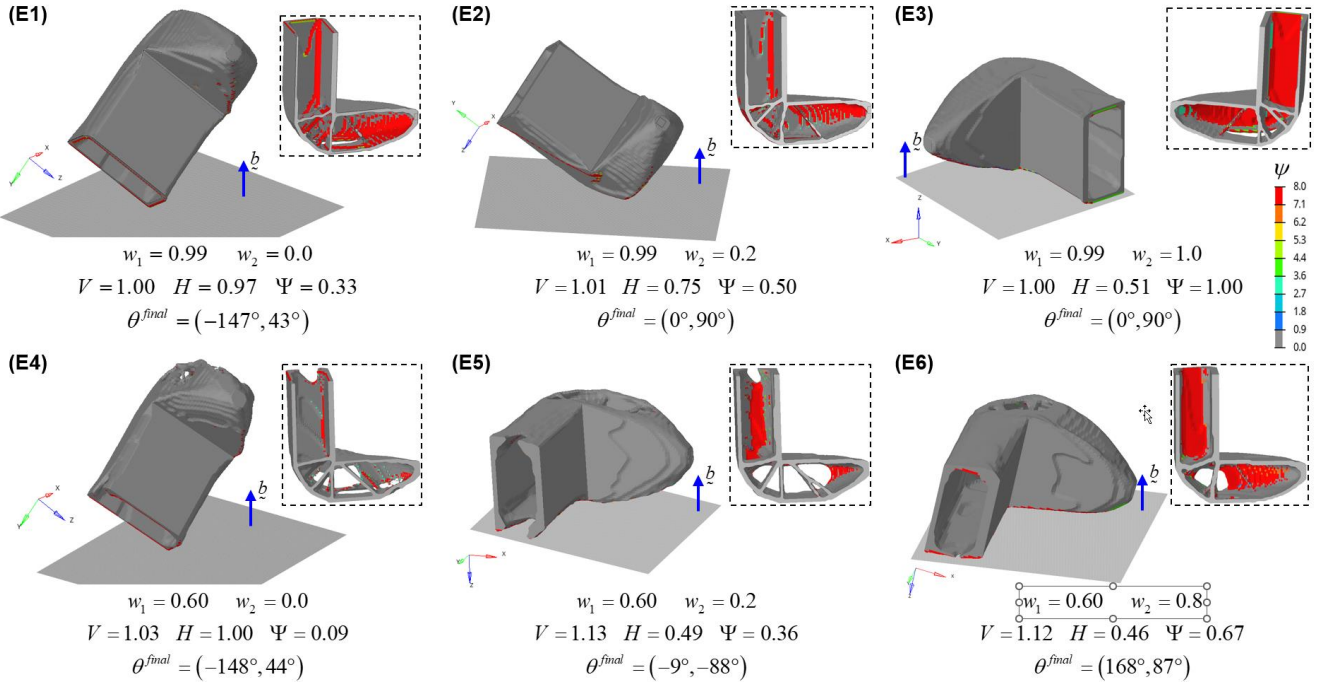


Figure 26 Summary of optimization results for the L-bracket problem when printing on a raft with various weighting factors.

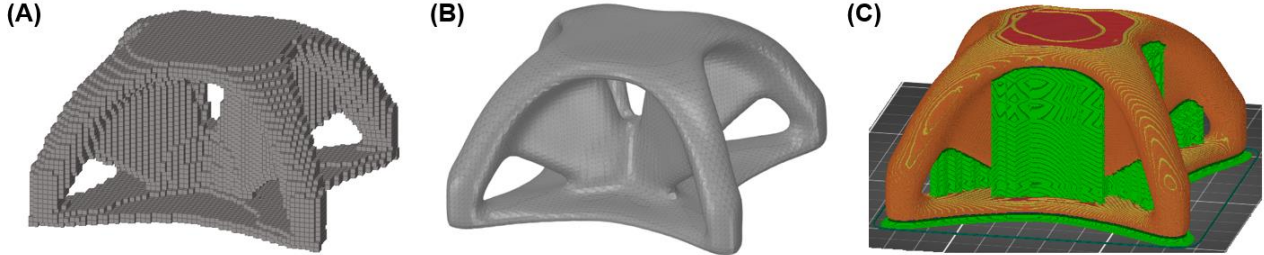


Figure 27 Example of the smoothing and slicing process used for verification of AM cost driving metrics, where (A) shows the thresholded physical density, (B) shows the smoothed .STL file, and (C) shows the slicer result with support structure.

The slicer verification results are summarized in Table 2, with optimization objectives included for reference using the same normalized values from the previous figures. The slicer metrics include print time, filament used (including part and support material), and support material interface, which is a factor that contributes to support structure removal cost. The printing time is influenced by both the build height and overhang area, while the filament used and support material interface are related only to the overhang area. The relative importance of each slicer metric will depend on many external factors such as the material used, printer model, cost of electricity, cost of labour, desired lead time, and overall importance of cost reduction compared to structural metrics.

For the cantilever beam model, the build height optimized designs (A5) and (B5) achieved 2 – 5% reductions in printing time, with 3 – 6% increases in filament used. These designs also had substantial increase in support material interface as designs (A1) and (B1) require essentially no support material. It should be noted that this table is comparing two results that are optimized for different AM cost metrics, rather than comparing an unoptimized and optimized result. The cantilever beam results show that optimizing for build height can reduce printing time even if the optimized design has increased overhang area. However, the reduction in build height achieved through optimization (~70% in these examples) is not directly proportional to the reduction in print time calculated through the slicer (~4% in these examples). This is to be expected because these designs decrease build

height but also increase overhang area, but even for models with identical overhang area, the relationship between build height and print time reduction is not expected to be 1:1. When selecting between these options, designs (A5) and (B5)

should be selected only if print time is very expensive. Otherwise, designs (A1) and (B1) are ideal due to their lower filament use, support material interface, and compliance.

Table 2 Comparison of optimization objectives and slicer metrics for cantilever, box, and L-bracket problems with multi-objective optimization

Model	Design	Relative Optimization Objectives			Relative Slicer Metrics		
		Compliance / Volume	Build Height	Overhang Area	Print Time	Filament Used	Support Material Interface
Cantilever (Raft)	(A1)	1.00	1.00	0.06	1.00	0.94	0.02
	(A5)	1.07	0.30	1.21	0.98	1.00	1.00
Cantilever (Build Plate)	(B1)	1.00	1.00	0.00	1.00	0.97	0.01
	(B5)	1.04	0.33	0.50	0.95	1.00	1.00
Simply Supported Box (Raft)	(C1)	1.00	1.00	0.31	1.00	0.92	0.38
	(C3)	1.00	0.55	0.97	0.91	1.00	1.00
	(C5)	1.01	0.96	0.19	0.84	0.81	0.22
	(C7)	1.03	0.43	0.41	0.61	0.79	0.47
Simply Supported Box (Build Plate)	(D1)	1.00	1.00	0.73	1.00	1.00	1.00
	(D3)	1.01	1.00	0.13	0.86	0.90	0.44
	(D4)	1.03	0.74	0.20	0.80	0.92	0.30
L-bracket (Raft)	(E1)	1.00	0.97	0.33	0.99	0.90	0.53
	(E3)	1.00	0.51	1.00	1.00	1.00	1.00
	(E4)	1.03	1.00	0.09	0.89	0.83	0.13
	(E5)	1.13	0.49	0.36	0.91	0.92	0.38

For the simply supported box problem when printing on a raft, a change in orientation to favour build height in (C3) as opposed to overhang area in (C1) resulted in a 9% reduction in print time with a 9% increase in filament used and a large increase in support material interface. Design (C5), which had an increased AM cost weighting while focusing only on overhang area, achieved a 16% reduction in print time and a 12% decrease in filament use relative to design (C1). By instead considering both overhang area and build height, design (C7) reduced print time by an additional 27% relative to (C5). These results show that the largest reduction in print time was achieved through a simultaneous reduction in both build height and overhang area. However, the reduction in optimization metrics cannot be directly translated to real-world cost reduction, as in this case a ~60% reduction in both build height and overhang area resulted in a 20 – 40% reduction in slicer metrics. When printing on a raft, design (C5) should be selected if there are large costs associated with support material removal, but otherwise design (C7) achieved the best reduction in both print time and filament use with only a 3% increase in compliance.

Similar trends were found for the simply supported box problem when printing on the build plate. The improvement

in optimization metrics did not directly translate to slicer metrics, with design (D3) achieving an 82% reduction in overhang area at the same build height as (D1) but with only a 14% decrease in print time and a 10% reduction in filament used. Considering overhang area and build height simultaneously reduced print time further than when considering only one objective, with design (D4) achieving a 7% reduction in print time relative to (D3). For this scenario, design (D4) is the best design with significant reductions in all slicer metrics with only a 3% increase in compliance.

With the L-bracket problem, designs (E1) and (E3) had only a 1% difference in print time, indicating the reduction in build height was counteracted by the increase in overhanging area. However, the overhang-focused result in (E1) is superior due the 10% lower filament use and 47% reduced support material interface. With a larger weighting on AM cost, designs (E4) and (E5) achieved about a 10% reduction in printing time. Design (E5), with a larger focus on build height, required a 13% increase in mass to achieve the reduction in print time, and resulted in more material use and support material interface than (E4). The build height reduction was again counteracted by the overhang area increase, indicating overhang area is the more important

objective for this problem. Design (E4) achieved the best results, with a 11% reduction in print time for a 3% mass increase.

The slicer metrics presented in this verification are only valid for FDM processes. When switching to other AM methods such as PBF or SLA, build height is expected to have a greater influence on printing time, because the dwell time between layers is more significant. For metal AM methods such as PBF, additional support structures are often required for thermal considerations, which would increase the print time, material use, and support material interface metrics. Therefore, the discussed trade-offs between slicer metrics are expected to change significantly for other AM methods, and the ideal design and build orientation would likely change.

## 4 Conclusions

This paper presented an approach for simultaneous topology and build orientation optimization using build height and overhang area as AM cost driving metrics. A novel methodology was formulated for build height optimization as a function of orientation design variables, and a base indicator field was introduced to enable overhang area minimization when printing on either the build plate or on a raft, to enable flexibility for different AM methods. Build height and overhang area were calculated using smooth continuous functions and sensitivity expressions were derived for gradient-based optimization. Build orientation initialization for 3D problems was addressed by automatically initializing the orientation design variables at an early TO iteration based on the desired trade-off between AM objectives, avoiding the need for the user to rerun optimization for multiple initial print orientations.

The proposed approach was applied to three 3D academic models with various combinations of problem statements and design variables to validate the functionality of the method and to gain new insights on the relationship between build height and overhang area. Topology optimization results with a single AM objective showed that build height minimization resulted in larger increases in structural compliance compared to overhang area minimization. This behaviour was expected because reducing the height of a component will often reduce the bending area moment of inertia, whereas overhangs can frequently be reduced through localized changes to the geometry. Build orientation optimization results often converged to clearly inferior local optimum solutions when starting from an arbitrary initial orientation, especially with build height and overhang area when printing on the build plate. The proposed automatic build orientation selection method converged to the best orientation obtained from the manual initializations and

achieved similar objective function values. The multi-objective optimization indicated a clear trade-off between overhang area and build height with respect to both topology and orientation. The orientation of the component had a significant impact on the reduction in build height and overhang area that could be achieved through TO and should be carefully selected based on the desired trade-offs between objectives. It was found that placing a small weighting factor on overhang area can help improve convergence behaviour as there will often be two orientations with equivalent height but very different overhanging features. Finally, the results showed the importance of distinguishing between printing on the build plate or printing on a raft, as results converged to very different orientations and geometry in some cases. When printing on the build plate, the optimization often resulted in designs with flat bottom surfaces that were raised away from the bottom of the design space to effectively reduce overhang area without sacrificing compliance, which is a behaviour that is not seen in current approaches in literature.

Optimized results were verified using a FDM slicer software, showing that the proposed methodology can yield up to a 27% reduction in printing time by simultaneously considering build height and overhang area rather than only overhang area. While these results are promising, the reductions in real-world cost metrics were less than the reduction in the AM objectives achieved during optimization. This is because the optimization uses a relatively simple AM cost model by considering only build height and overhang area. A more complete cost model would include other physical properties such as support structure volume and surface area in the optimization. The estimation of support material removal costs should also be improved to consider tooling accessibility. In addition, more detailed investigation and slicer verification is needed to understand the relative importance of each AM cost driving physical property, which is expected to change significantly for other AM processes, such as BPF or SLA. Another limitation of this approach is that it assumes a single part is being printed in the build volume, whereas manufacturers may often reduce AM cost by printing many components in a single batch and would orient components accordingly. Besides AM cost, a topology and build orientation optimization tool should also include constraints such as the size of the component within the printer volume and limits on the thermal stresses and deformations in metal AM to ensure successful prints.

## Compliance with ethical standards

**Conflict of interest** The authors declare that they have no conflict of interest.

**Funding** This research was funded by the Natural Sciences and Engineering Research Council of Canada (NSERC).

**Replication of results** Sufficient information is provided for replication of the results presented within this paper. All parameter settings and implementation aspects have been described in detail and appropriate references are included for aspects outside of the scope of the paper. A pseudo code is provided in Appendix E for further clarification.

## Appendix A: Sensitivity Analysis

Gradient-based optimization requires the sensitivities of objective and constraint functions to update design variable values. These sensitivities are derived in the following sections with respect to element density and orientation design variables and are verified through finite differencing.

The sensitivity analysis of compliance when using an external FE solver is discussed in detail by Roper et al. (Roper et al. 2019) and can be expressed as a function of the compliance  $C_e$  of the  $e$ -th element as follows:

$$\frac{\partial C}{\partial \rho_e} = -\frac{C_e}{E_e} \frac{\partial E_e}{\partial \rho_e} = \left( \frac{E_{\min}}{E_e} - 1 \right) \frac{p}{\rho_e} C_e. \quad (27)$$

### A.1 Physical Densities

In this work, the sensitivities of objectives and constraints are derived in terms of the physical densities. These sensitivities must therefore be adjusted to be expressed in terms of the element density design variables. This process is illustrated for a generic response as

$$\frac{\partial \square}{\partial x_i} = \sum_{e \in N_i} \frac{\partial \square}{\partial \rho_e} \frac{\partial \rho_e}{\partial \tilde{x}_e} \frac{\partial \tilde{x}_e}{\partial x_i} \quad (28)$$

where sensitivities are summed for all neighbouring elements belonging to  $N_i$  and are multiplied by the sensitivity terms of the filtered and thresholded density as follows:

$$\frac{\partial \tilde{x}_e}{\partial x_i} = \frac{w_{ei} v_i}{\sum_{i \in N_e} w_{ei} v_i} \quad (29)$$

$$\frac{\partial \rho_e}{\partial \tilde{x}_e} = \beta_\rho \frac{1 - \tanh^2(\beta_\rho (\tilde{x}_e - \eta_\rho))}{\tanh(\beta_\rho \eta_\rho) + \tanh(\beta_\rho (1 - \eta_\rho))} \quad (30)$$

### A.2 Build Direction Vector

The sensitivity of the build direction vector with respect to the  $k$ -th orientation design variable can be expressed as

$$\frac{\partial \tilde{b}}{\partial \theta_k} = \frac{\partial \tilde{R}}{\partial \theta_k} \tilde{b} \quad (31)$$

where the rotation matrix partial derivatives are expressed as follows:

$$\frac{\partial \tilde{R}}{\partial \theta_1} = \begin{bmatrix} -\sin \theta_1 & -\cos \theta_1 & 0 \\ \cos \theta_2 \cos \theta_1 & -\cos \theta_2 \sin \theta_1 & 0 \\ \sin \theta_2 \cos \theta_1 & -\sin \theta_2 \sin \theta_1 & 0 \end{bmatrix} \quad (32)$$

$$\frac{\partial \tilde{R}}{\partial \theta_2} = \begin{bmatrix} 0 & 0 & 0 \\ -\sin \theta_2 \sin \theta_1 & -\sin \theta_2 \cos \theta_1 & -\cos \theta_2 \\ \cos \theta_2 \sin \theta_1 & \cos \theta_2 \cos \theta_1 & -\sin \theta_2 \end{bmatrix} \quad (33)$$

### A.3 Build Height – Density

The sensitivity of build height with respect to physical densities can be expressed as a simple addition of the sensitivities of the top and bottom distances, which can be expanded using the chain rule as

$$\frac{\partial H}{\partial \rho_e} = \frac{\partial T}{\partial \rho_e} - \frac{\partial B}{\partial \rho_e} = \sum_{i \in N} \frac{\partial S_{MAX}}{\partial \hat{h}_i} \frac{\partial \hat{h}_i}{\partial \rho_e} - \sum_{i \in N} \frac{\partial S_{MIN}}{\partial \hat{h}_i} \frac{\partial \hat{h}_i}{\partial \rho_e} \quad (34)$$

where the partial derivative of the smooth maximum and minimum functions with respect to a generic input  $c_i$  is calculated as:

$$\frac{\partial S}{\partial c_i} = \frac{e^{\alpha c_i}}{\sum_{i \in N} e^{\alpha c_i}} (1 + \alpha(c_i - S)) \quad (35)$$

The physical density of any given element influences the height centroid of the component, and therefore affects the  $\hat{h}_e$  distance term of all other elements in Equation (13). Therefore, the summations in Equation (34) must be included to consider the effect of the  $e$ -th physical density on the  $i$ -th distance term. These sensitivity terms are derived as follows:

$$\frac{\partial \hat{h}_i}{\partial \rho_e} = (h_i - \bar{h}) \frac{\rho_i^{1/p-1}}{p} \delta_{ie} - \frac{\bar{h}}{\partial \rho_e} \rho_i^{1/p} \quad (36)$$

where  $\delta_{ij}$  is the Kronecker delta, which is equal to one when  $i = e$ , and zero otherwise.

The last term needed to compute the sensitivity of build height with respect to the physical densities is the partial derivative of the height centroid is expressed as:

$$\frac{\partial \bar{h}}{\partial \rho_e} = \frac{\rho_e^{1/p-1}}{p \sum_{i \in N} \rho_i^{1/p}} (h_e - \bar{h}) \quad (37)$$

### A.4 Build Height – Orientation

The build height sensitivity with respect to the build orientation can be derived in a similar way, starting with the addition of top and bottom distance sensitivities as

$$\frac{\partial H}{\partial \theta_k} = \frac{\partial T}{\partial \theta_k} - \frac{\partial B}{\partial \theta_k} = \sum_{i \in N} \frac{\partial S_{MAX}}{\partial \hat{h}_i} \frac{\partial \hat{h}_i}{\partial \theta_k} - \sum_{i \in N} \frac{\partial S_{MIN}}{\partial \hat{h}_i} \frac{\partial \hat{h}_i}{\partial \theta_k} \quad (38)$$

where the sensitivity of the vertical distance term from the height centroid is derived as follows:

$$\frac{\partial \hat{h}_i}{\partial \theta_k} = \left( \frac{\partial h_i}{\partial \theta_k} - \frac{\partial \bar{h}}{\partial \theta_k} \right) \rho_i^{1/p} \quad (39)$$

The partial derivative of the height centroid with respect to build orientation is evaluated using a summation of chain rule terms as:

$$\frac{\partial \bar{h}}{\partial \theta_k} = \frac{1}{\sum_{i \in N} \rho_i^{1/p}} \sum_{i \in N} \rho_i^{1/p} \frac{\partial h_i}{\partial \theta_k} \quad (40)$$

Finally, the sensitivity of element height with respect to orientation is calculated as:

$$\frac{\partial h_i}{\partial \theta_k} = \underline{r}_i \cdot \frac{\partial \underline{b}}{\partial \theta_k} \quad (41)$$

## A.5 Overhang Area – Density

The sensitivity of component overhang area is expressed as a summation of the partial derivatives of each element's surface area with respect to the physical density of the element of interest as

$$\frac{\partial \Psi}{\partial \rho_i} = \sum_{e \in N} \frac{\partial \psi_e}{\partial \rho_i} \quad (42)$$

where the partial derivative term is calculated using the chain rule as:

$$\frac{\partial \psi_e}{\partial \rho_i} = \frac{\partial \bar{\psi}_e}{\partial \rho_i} \phi_e \mu_e + \bar{\psi}_e \frac{\partial \phi_e}{\partial \rho_i} \mu_e + \bar{\psi}_e \phi_e \frac{\partial \mu_e}{\partial \rho_i} \quad (43)$$

The partial derivatives of the smooth Heaviside functions for build plate indicator, overhang indicator, and element surface area are calculated as follows:

$$\frac{\partial \mu_e}{\partial \rho_i} = \begin{cases} 0, & \text{raft} \\ \frac{\beta_\mu \left[ 1 - \tanh^2(\beta_\mu (h_e - \bar{h} - B - \eta_\mu)) \right]}{\tanh(\beta_\mu (1 + \eta_\mu)) + \tanh(\beta_\mu (1 - \eta_\mu))} \left( -\frac{\partial \bar{h}}{\partial \rho_i} - \frac{\partial B}{\partial \rho_i} \right), & \text{buildplate} \end{cases} \quad (44)$$

$$\frac{\partial \bar{\psi}_e}{\partial \rho_i} = \frac{\beta_\psi \left[ 1 - \tanh^2(\beta_\psi (\cos \alpha_e - \eta_\psi)) \right]}{\tanh(\beta_\psi (1 + \eta_\psi)) + \tanh(\beta_\psi (1 - \eta_\psi))} \frac{\partial \cos \alpha_e}{\partial \rho_i} \quad (45)$$

$$\frac{\partial \phi_e}{\partial \rho_i} = \beta_\phi \frac{v_e^{2/3}}{a} \left( \frac{1 - \tanh^2(\beta_\phi (\|\nabla \rho_e\| - \eta_\phi))}{2 \tanh(\beta_\phi \eta_\phi)} \right) \frac{\partial \|\nabla \rho_e\|}{\partial \rho_i} \quad (46)$$

The bottom and height centroid partial derivatives in Equation (44) are outlined in Section A1.3 and are valid for all  $e$ -th and  $i$ -th elements. The partial derivative of the cosine of the angle between the spatial gradient vector and build direction vector is expressed as

$$\frac{\partial \cos \alpha_e}{\partial \rho_i} = \frac{1}{\|\nabla \rho_e\| + \varepsilon} \left( \frac{\partial (\nabla \rho_e) \cdot \underline{b}}{\partial \rho_i} \right) - \frac{(\nabla \rho_e \cdot \underline{b})}{(\|\nabla \rho_e\| + \varepsilon)^2} \frac{\partial \|\nabla \rho_e\|}{\partial \rho_i} \quad (47)$$

where the spatial gradient magnitude and spatial gradient vector partial derivatives are derived as follows:

$$\frac{\partial \|\nabla \rho_e\|}{\partial \rho_i} = \frac{\nabla \rho_e}{\|\nabla \rho_e\| + \varepsilon} \cdot \frac{\partial (\nabla \rho_e)}{\partial \rho_i} \quad (48)$$

$$\frac{\partial (\nabla \rho_e)}{\partial \rho_i} = \frac{v_i s_{ei}}{\sum_{i \in N_e} \|s_{ei}\| v_i} \quad (49)$$

These spatial gradient sensitivities are valid when the  $i$ -th element exists within the  $e$ -th element's interface radius and are zero for all other elements.

## A.6 Overhang Area – Orientation

The partial derivative of overhang area with respect to orientation design variables is expressed as

$$\frac{\partial \Psi}{\partial \theta_k} = \sum_{e \in N} \frac{\partial \psi_e}{\partial \theta_k} \quad (50)$$

where the partial derivative of element overhang area is calculated as:

$$\frac{\partial \psi_e}{\partial \theta_k} = \frac{\partial \bar{\psi}_e}{\partial \theta_k} \phi_e \mu_e + \bar{\psi}_e \phi_e \frac{\partial \mu_e}{\partial \theta_k} \quad (51)$$

The surface area term is not a function of orientation, while the build indicator and overhang indicator partial derivatives are as follows:

$$\frac{\partial \mu_e}{\partial \theta_k} = \begin{cases} 0, & \text{raft} \\ \frac{\beta_\mu \left[ 1 - \tanh^2(\beta_\mu (h_e - \bar{h} - B - \eta_\mu)) \right]}{\tanh(\beta_\mu (1 + \eta_\mu)) + \tanh(\beta_\mu (1 - \eta_\mu))} \left( \frac{\partial h_e}{\partial \theta_k} - \frac{\partial \bar{h}}{\partial \theta_k} - \frac{\partial B}{\partial \theta_k} \right), & \text{build plate} \end{cases} \quad (52)$$

$$\frac{\partial \bar{\psi}_e}{\partial \theta_k} = \frac{\beta_\psi \left[ 1 - \tanh^2(\beta_\psi (\cos \alpha_e - \eta_\psi)) \right]}{\tanh(\beta_\psi (1 + \eta_\psi)) + \tanh(\beta_\psi (1 - \eta_\psi))} \frac{\partial \cos \alpha_e}{\partial \theta_k} \quad (53)$$

The bottom, height centroid, and element height partial derivatives with respect to orientation are derived in Section A1.4, whereas the partial derivative of the cosine of the angle between the spatial gradient and the build orientation vector is calculated as:

$$\frac{\partial \cos \alpha_e}{\partial \theta_k} = \frac{\nabla \tilde{\rho}_e}{\|\nabla \tilde{\rho}_e\| + \varepsilon} \cdot \frac{\partial \tilde{b}}{\partial \theta_k} \quad (54)$$

### A.7 Sensitivity Verification

The finite difference (FD) method was used to verify the analytical sensitivities derived for build height and overhang area as a function of physical density and orientation. FD sensitivities were calculated for a 2D cantilever beam model with 4000 elements at iteration 5 of a topology optimization solution. The physical density field and build direction vector corresponding to  $\theta_l = -5^\circ$  are shown in Figure 28. Table 3 summarizes the sensitivity verification for orientation design variables with a step size of  $\Delta\theta = 0.001 \text{ rad} \approx 0.06^\circ$ , while Table 4 shows sensitivity verification for 15 randomly selected elements with a step size of  $\Delta\rho = 10^{-6}$ . Results show excellent agreement between the FD and analytical sensitivities.

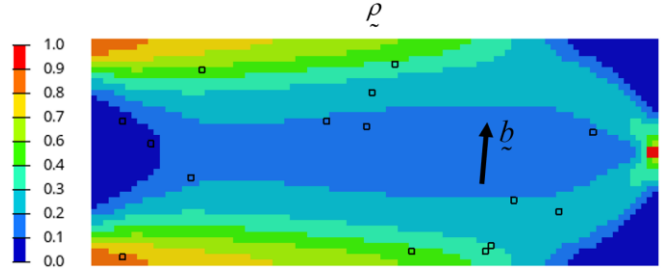


Figure 28 Intermediate topology optimization densities and build orientation used for FD sensitivity verification, with randomly selected elements indicated in boxes.

Table 3 Sensitivity verification for build orientation design variable

Objective (□)	FD $\Delta\square/\Delta\theta_l$	Analytical $\partial\square/\partial\theta_l$	$\frac{\Delta\square/\Delta\theta_l}{\partial\square/\partial\theta_l} \times 100\%$
Build Height ( $H$ )	-35.3710	-35.3726	99.995%
Overhang Area ( $\Psi$ )	11.5257	11.5245	100.010%

Table 4 Sensitivity verification for element physical density

Element $e$	Height			Overhang Area		
	FD $\Delta H/\Delta\rho_e \times 10^3$	Analytical $\partial H/\partial\rho_e \times 10^3$	$\frac{\Delta H/\Delta\rho_e}{\partial H/\partial\rho_e} \times 100\%$	FD $\Delta\Psi/\Delta\rho_e$	Analytical $\partial\Psi/\partial\rho_e$	$\frac{\Delta H/\Delta\rho_e}{\partial\Psi/\partial\rho_e} \times 100\%$
2992	0.37891	0.37891	100.000%	-0.47236	-0.47236	100.000%
3839	17.29863	17.29864	100.000%	-0.34639	-0.34639	100.000%
929	0.57286	0.57285	99.998%	-0.07851	-0.07851	100.000%
1259	-0.45932	-0.45932	100.000%	0.00000	0.00000	-
1370	-0.90889	-0.90888	99.999%	0.62150	0.62150	100.000%
2887	0.35328	0.35327	99.997%	-0.47963	-0.47963	100.000%
3466	-0.21988	-0.21988	100.000%	-0.63758	-0.63758	100.000%
2758	0.65387	0.65387	100.000%	-0.07338	-0.07338	100.000%
1378	-0.96066	-0.96065	99.999%	0.31151	0.31151	100.000%
3502	-0.27459	-0.27458	99.996%	0.53177	0.53177	100.000%
1613	-3.10416	-3.10416	100.000%	0.52600	0.52600	100.000%
3991	0.30119	0.30119	100.000%	-0.04239	-0.04239	100.000%
1125	-1.19885	-1.19886	100.001%	0.19172	0.19172	100.000%
156	-0.51054	-0.51056	100.004%	0.36914	0.36914	100.000%
3235	-0.56609	-0.56609	100.000%	-0.00002	-0.00002	100.000%

## Appendix B: Comparison to Approaches from Literature

The proposed multi-objective compliance minimization approach was compared to two examples from literature using the same geometry, number of elements, volume fraction, and filter radius described in the respective publications.

Figure 29 compares to the discrete truss-based optimization from (Mass and Amir 2017). The baseline design in (A) was essentially fully printable in the print direction from (B), so very little design changes were needed in (B). The proposed method shows superior performance in print direction (C), where the design achieved a 0.1% unprintability metric (UP) (Mass and Amir 2017) with only a 1% increase in compliance, compared to the 12% increase in compliance and 14.6% UP result from Mass and Amir.

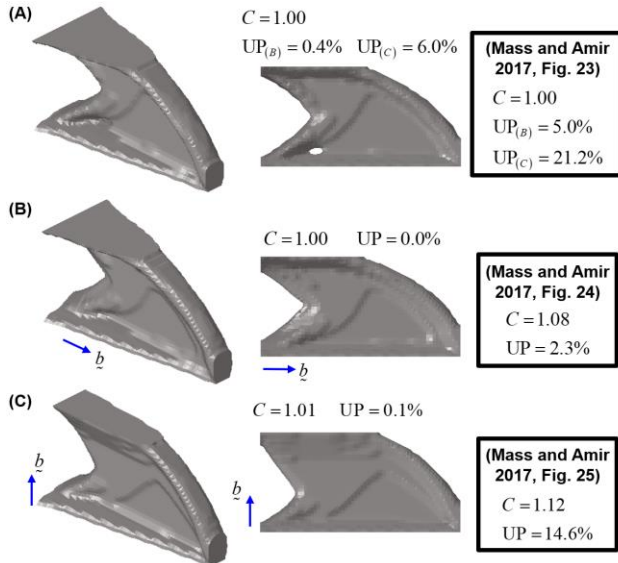


Figure 29 Comparison of proposed method to discrete truss-based optimization from (Mass and Amir 2017).

Figure 30 shows a comparison to the projection method from (Langelaar 2016b) that eliminates unprintable elements from the compliance calculation. The infeasible overhanging surface fraction  $\Pi$  (Langelaar 2016b) is calculated for each result. Nearly identical performance was seen for build orientations (A) and (B). In orientation (C), the Langelaar approach used many finger-like structures to build upwards from the bottom of the design space to support the web of the beam. These design features cannot be achieved with the proposed method because the interface filter continuation scheme is explicitly formulated to avoid the dripping or boundary oscillation effect. The design in (C) instead reduced the overhanging metric from 17% to 8% with a 5% increase in compliance, compared to the 7% increase in

compliance from the Langelaar design. In orientation (D), the proposed approach produced an overhang free design with a 7% increase in compliance, whereas Langelaar produced a self-supporting design without any compliance increase.

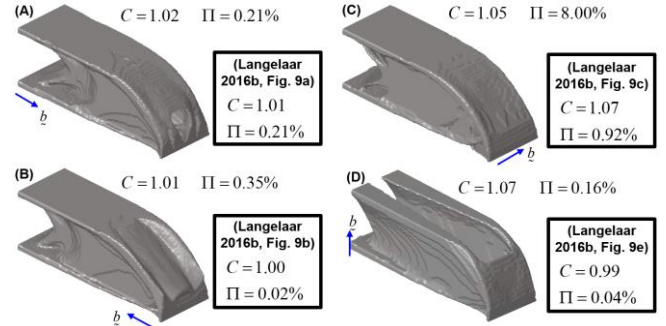


Figure 30 Comparison of proposed method to the AM filter from (Langelaar 2016b).

## Appendix C: Convergence History

Convergence plots for simultaneous topology and build orientation optimization are included for standard orientation initialization in Figure 31 and for the automatic orientation initialization in Figure 32. These results, normalized relative to each other, show that the standard orientation initialization drastically reduced overhang area in the first 10 iterations as the orientation of the part changed. The automatic initialization considered only compliance until iteration 5, then initialized the orientation design variables at  $\theta = (90^\circ, 90^\circ)$ , resulting in a lower overhang area objective compared to the standard initialization of  $\theta = (0^\circ, 0^\circ)$  at iteration 0. There are no overhang area objective values in Figure 32 (A) before build orientation initialization.

Optimization history is included for the multi-objective stiffness constrained L-bracket problem in Figure 33. All objectives in (A) decreased within each phase, with sharp changes occurring when the optimization parameters were adjusted. In this example, the orientation design variables in (B) shifted from the automatic initialization at  $\theta = (180^\circ, 90^\circ)$  to  $\theta = (189^\circ, 92^\circ)$  by the end of the optimization. The displacements responses in (C) briefly violated the constraint limits at the start of the second phase but otherwise remained within the feasible range.

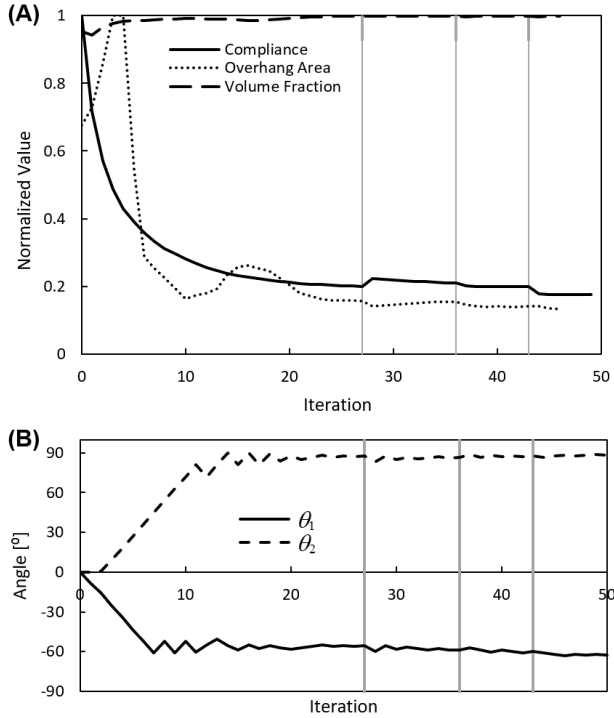


Figure 31 Convergence history for result (B1) from Figure 19. Solid vertical lines indicate the beginning of a new phase.

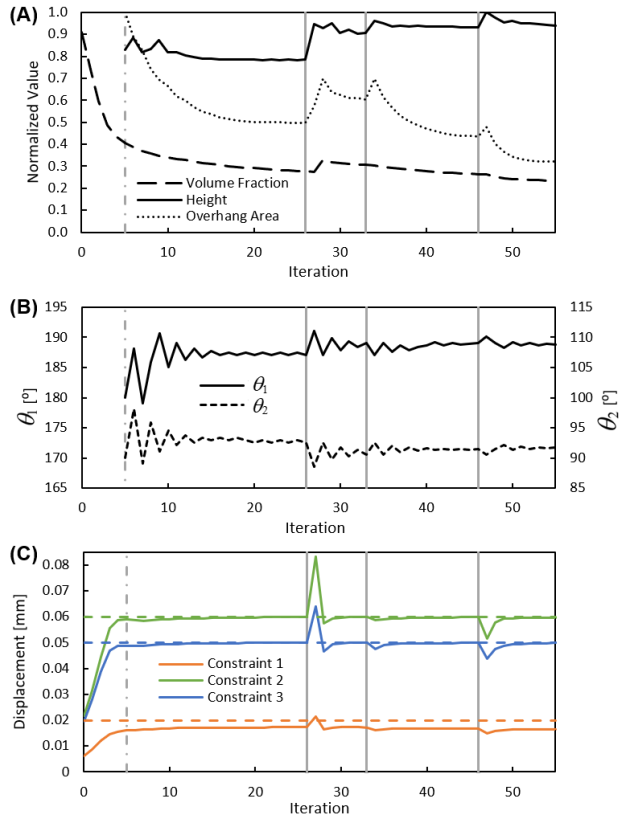


Figure 33 Convergence history for result (E5) from Figure 26. The coloured horizontal lines indicate the respective constraint limits.

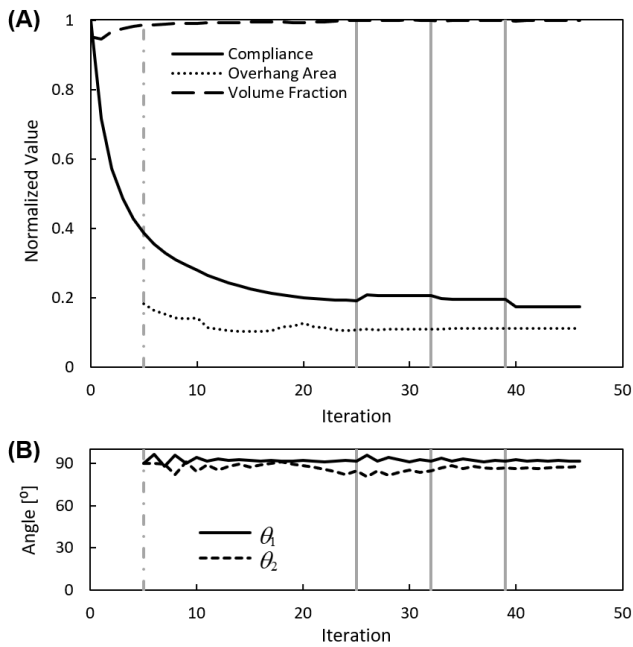


Figure 32 Convergence history for result (B5) from Figure 19. The dotted vertical line indicates the build orientation initialization stage.

## Appendix D: Slicer Settings

The slicer verification was completed in PrusaSlicer v2.5.0 for the “Original Prusa i3 MK3S & MK3S+” printer with “Generic PLA” filament and the default “0.20 mm QUALITY” print settings with the modifications outlined in Table 5. The cantilever beam, simply supported box, and L-bracket results were scaled to 5%, 10%, and 50%, respectively, of their original size to fit within the printer build volume. Relative Print Time was calculated from “Estimated printing time - normal mode”, Relative Filament Used was calculated from “Used Filament (g)”, and Relative Support Material Interface was calculated from “Feature type - Support Material Interface - Used filament (g)”.

Table 5: Changes from “0.20 mm QUALITY” default print settings

Setting	Value
Generate Support Material	YES
Overhang Threshold	45°
Support Material Style	Snug
Fill Density	100
Fill Pattern	Rectilinear
Perimeters	4
Raft Layers (if building on raft)	3

## Appendix E: Pseudo Code

! Pseudocode providing structure of approach

### PROGRAM MAIN

! Define key variables for pseudocode

**INTEGER** :: PHASE = 1 ! opt. parameters based on this

**LOGICAL** :: CONVERGE = .FALSE. ! is opt. converged?

**LOGICAL** :: THETA = .FALSE. ! is orientation active?

! Read model and optimization settings

**CALL** READ\_SETTINGS

! Initialize design variables and optimization parameters

**CALL** INITIALIZE

! Main optimization loop

**DO** I = 1, MAX\_ITER ! max. number of iterations

! Initialize orientation at selected iteration

**IF** (I == 5) **CALL** ORIENTATION\_SEARCH(THETA)

! Filter element densities

**CALL** DENSITY\_FILTER(PHASE)

! Update Young's modulus

**CALL** STIFFNESS\_INTERP(PHASE)

! Run OptiStruct finite element analysis

**CALL** RUN\_FEA

! Calculate compliance and sensitivities

**CALL** COMPLIANCE\_CALC(PHASE)

! Calculate build height, overhang area, and sensitivities

**CALL** AM\_OBJECTIVE\_CALC(PHASE,THETA)

! Calculate volume fraction constraint and sensitivities

**CALL** VOL\_FRAC\_CALC(PHASE)

! Adjust sensitivities based on filtering scheme

**CALL** SENSITIVITY\_ADJUST(PHASE)

! Update design variable values

**CALL** DV\_UPDATE(THETA)

! Check for optimization convergence

**CALL** CHECK\_CONVERGENCE(CONVERGE)

**IF** (CONVERGE) PHASE = PHASE + 1

**IF**(PHASE > 4) **EXIT**

**END DO**

### END PROGRAM MAIN

## References

- Allaire, G, Dapogny, C, Estevez, R, Faure, A, Michailidis, G (2017) Structural optimization under overhang constraints imposed by additive manufacturing technologies. *J Comput Phys* 351:295-328. <https://doi.org/10.1016/j.jcp.2017.09.041>
- Bendsoe, MP, Sigmund, O (2003) Topology Optimization: Theory, Methods, and Applications, Springer Berlin, Heidelberg
- Chen, H, Joglekar, A, Whitefoot, KS, Burak Kara, L (2023) Concurrent Build Direction, Part Segmentation, and Topology Optimization for Additive Manufacturing Using Neural Networks. *J Mech Des* 145(9). <https://doi.org/10.1115/1.4062663>
- Cheng, L, To, A (2019) Part-scale build orientation optimization for minimizing residual stress and support volume for metal additive manufacturing: Theory and experimental validation. *Comput Aided Des* 113:1-23. <https://doi.org/https://doi.org/10.1016/j.cad.2019.03.004>
- Clausen, A, Andreassen, E (2017) On filter boundary conditions in topology optimization. *Struct Multidiscip Optim* 56(5):1147-1155. <https://doi.org/10.1007/s00158-017-1709-1>
- Crispo, L, Bohrer, R, Roper, SWK, Kim, IY (2021) Spatial gradient interface detection in topology optimization for an unstructured mesh. *Struct Multidiscip Optim* 63(1):515-522. <https://doi.org/10.1007/s00158-020-02688-z>
- Crispo, L, Kim, IY (2021) Part consolidation for additive manufacturing: A multilayered topology optimization approach. *Int J Numer Methods Eng* 122(18):4987-5027. <https://doi.org/10.1002/nme.6754>
- Deaton, JD, Grandhi, RV (2014) A survey of structural and multidisciplinary continuum topology optimization: post 2000. *Struct Multidiscip Optim* 49(1):1-38. <https://doi.org/10.1007/s00158-013-0956-z>
- Delfs, P, Tows, M, Schmid, HJ (2016) Optimized build orientation of additive manufactured parts for improved surface quality and build time. *Addit Manuf* 12:314-320. <https://doi.org/10.1016/j.addma.2016.06.003>
- Fritz, K, Kim, IY (2020) Simultaneous topology and build orientation optimization for minimization of additive manufacturing cost and time. *Int J Numer Methods Eng* 121(15):3442-3481. <https://doi.org/10.1002/nme.6366>
- Gao, W, Zhang, YB, Ramanujan, D, Ramani, K, Chen, Y, Williams, CB, Wang, CCL, Shin, YC, Zhang, S, Zavattieri, PD (2015) The status, challenges, and future of additive manufacturing in engineering. *Comput Aided Des* 69:65-89. <https://doi.org/10.1016/j.cad.2015.04.001>
- Garaigordobil, A, Ansola, R, de Bustos, IF (2021) On preventing the dripping effect of overhang constraints in topology optimization for additive manufacturing. *Struct Multidiscip Optim* 64(6):4065-4078. <https://doi.org/10.1007/s00158-021-03077-w>
- Garaigordobil, A, Ansola, R, Santamaria, J, de Bustos, IF (2018) A new overhang constraint for topology optimization of self-supporting structures in additive manufacturing. *Struct Multidiscip Optim* 58(5):2003-2017. <https://doi.org/10.1007/s00158-018-2010-7>
- Gaynor, AT, Guest, JK (2016) Topology optimization considering overhang constraints: Eliminating sacrificial support material in additive manufacturing through design. *Struct Multidiscip Optim* 54(5):1157-1172. <https://doi.org/10.1007/s00158-016-1551-x>
- Guo, X, Zhou, JH, Zhang, WS, Du, ZL, Liu, C, Liu, Y (2017) Self-supporting structure design in additive manufacturing through explicit topology optimization. *Comput Methods Appl Mech Eng* 323:27-63. <https://doi.org/10.1016/j.cma.2017.05.003>
- Huang, RZ, Riddle, M, Graziano, D, Warren, J, Das, S, Nimbalkar, S, Cresko, J, Masanet, E (2016) Energy and emissions saving potential of additive manufacturing: the case of lightweight aircraft components. *J Clean Prod* 135:1559-1570. <https://doi.org/10.1016/j.jclepro.2015.04.109>

- Kekre, HB, Gcharge, SM (2010) Image Segmentation using Extended Edge Operator for Mammographic Images. *Int J Comput Sci Eng* 2(4):1086-1091.
- Kuo, YH, Cheng, CC (2019) Self-supporting structure design for additive manufacturing by using a logistic aggregate function. *Struct Multidiscip Optim* 60(3):1109-1121. <https://doi.org/10.1007/s00158-019-02261-3>
- Langelaar, M (2016a) Topology optimization for additive manufacturing with controllable support structure costs. In: Proceedings of the European Congress on Computational Methods in Applied Sciences and Engineering, Greece, pp. 3689-3699
- Langelaar, M (2016b) Topology optimization of 3D self-supporting structures for additive manufacturing. *Addit Manuf* 12:60-70. <https://doi.org/10.1016/j.addma.2016.06.010>
- Langelaar, M (2018) Combined optimization of part topology, support structure layout and build orientation for additive manufacturing. *Struct Multidiscip Optim* 57(5):1985-2004. <https://doi.org/10.1007/s00158-017-1877-z>
- Leary, M, Merli, L, Torti, F, Mazur, M, Brandt, M (2014) Optimal topology for additive manufacture: A method for enabling additive manufacture of support-free optimal structures. *Mater Des* 63:678-690. <https://doi.org/10.1016/j.matdes.2014.06.015>
- Liu, JK, Chen, Q, Liang, X, To, AC (2019) Manufacturing cost constrained topology optimization for additive manufacturing. *Front Mech Eng* 14(2):213-221. <https://doi.org/10.1007/s11465-019-0536-z>
- Liu, JK, Gaynor, AT, Chen, SK, Kang, Z, Suresh, K, Takezawa, A, Li, L, Kato, J, Tang, JY, Wang, CCL, Cheng, L, Liang, X, To, AC (2018) Current and future trends in topology optimization for additive manufacturing. *Struct Multidiscip Optim* 57(6):2457-2483. <https://doi.org/10.1007/s00158-018-1994-3>
- Liu, ST, Li, QH, Chen, WJ, Tong, LY, Cheng, GD (2015) An identification method for enclosed voids restriction in manufacturability design for additive manufacturing structures. *Front Mech Eng* 10(2):126-137. <https://doi.org/10.1007/s11465-015-0340-3>
- Liu, YC, Zhou, MD, Wei, C, Lin, ZQ (2021) Topology optimization of self-supporting infill structures. *Struct Multidiscip Optim* 63(5):2289-2304. <https://doi.org/10.1007/s00158-020-02805-y>
- Mass, Y, Amir, O (2017) Topology optimization for additive manufacturing: Accounting for overhang limitations using a virtual skeleton. *Addit Manuf* 18:58-73. <https://doi.org/10.1016/j.addma.2017.08.001>
- Matos, MA, Rocha, A, Pereira, AI (2020) Improving additive manufacturing performance by build orientation optimization. *Int J Adv Manuf Technol* 107(5-6):1993-2005. <https://doi.org/10.1007/s00170-020-04942-6>
- Meisel, N, Williams, C (2015) An Investigation of Key Design for Additive Manufacturing Constraints in Multimaterial Three-Dimensional Printing. *J of Mech Des* 137(1):1. <https://doi.org/10.1115/1.4030991>
- Mhapsekar, K, McConaha, M, Anand, S (2018) Additive Manufacturing Constraints in Topology Optimization for Improved Manufacturability. *J Manuf Sci Eng* 140(5):1-16. <https://doi.org/10.1115/1.4039198>
- Mirzendehdel, AM, Suresh, K (2016) Support structure constrained topology optimization for additive manufacturing. *Comput Aided Des* 81:1-13. <https://doi.org/10.1016/j.cad.2016.08.006>
- Olsen, J, Kim, IY (2020) Design for additive manufacturing: 3D simultaneous topology and build orientation optimization. *Struct Multidiscip Optim* 62(4):1989-2009. <https://doi.org/10.1007/s00158-020-02590-8>
- Pandey, PM, Thrimurthulu, K, Reddy, NV (2004) Optimal part deposition orientation in FDM by using a multicriteria genetic algorithm. *Int J Prod Res* 42(19):4069-4089. <https://doi.org/10.1080/00207540410001708470>
- Phatak, AM, Pande, SS (2012) Optimum part orientation in Rapid Prototyping using genetic algorithm. *J Manuf Syst* 31(4):395-402. <https://doi.org/10.1016/j.jmsy.2012.07.001>
- Qian, XP (2017) Undercut and overhang angle control in topology optimization: A density gradient based integral approach. *Int J Numer Methods Eng* 111(3):247-272. <https://doi.org/10.1002/nme.5461>
- Ranjan, R, Samant, R, Anand, S (2017) Integration of Design for Manufacturing Methods With Topology Optimization in Additive Manufacturing. *J Manuf Sci Eng* 139(6). <https://doi.org/10.1115/1.4035216>
- Roper, S, Vierhout, G, Li, D, Sangha, B, Pamwar, M, Kim, IY (2019) Multi-Material Topology Optimization and Multi-Material Selection in Design. In: Proceedings of the WCX SAE World Congress Experience, Detroit, MI, pp. 1-12
- Ryan, L, Kim, IY (2019) A multiobjective topology optimization approach for cost and time minimization in additive manufacturing. *Int J Numer Methods Eng* 118(7):371-394. <https://doi.org/10.1002/nme.6017>
- Sabiston, G, Kim, IY (2019) 3D topology optimization for cost and time minimization in additive manufacturing. *Struct Multidiscip Optim* 61(2):731-748. <https://doi.org/10.1007/s00158-019-02392-7>
- Schmitt, M, Kim, IY (2021) Topology optimization for infill in MEx. *Rapid Prototyp J* 27(8):1580-1590. <https://doi.org/10.1108/rpj-02-2021-0029>
- Sigmund, O (2007) Morphology-based black and white filters for topology optimization. *Struct Multidiscip Optim* 33:401-424. <https://doi.org/10.1007/s00158-006-0087-x>
- Sigmund, O (2022) On benchmarking and good scientific practise in topology optimization. *Struct Multidiscip Optim* 65(11):315. <https://doi.org/10.1007/s00158-022-03427-2>
- Svanberg, K (1987) The Method of Moving Asymptotes - a New Method for Structural Optimization. *Int J Numer Methods Eng* 24(2):359-373. <https://doi.org/10.1002/nme.1620240207>
- Thompson, MK, Moroni, G, Vaneker, T, Fadel, G, Campbell, RI, Gibson, I, Bernard, A, Schulz, J, Graf, P, Ahuja, B, Martina, F (2016) Design for Additive Manufacturing: Trends, opportunities, considerations, and constraints. *Cirp Ann - Manuf Techn* 65(2):737-760. <https://doi.org/10.1016/j.cirp.2016.05.004>
- Thore, CJ, Grundstrom, HA, Torstenfelt, B, Klarbring, A (2019) Penalty regulation of overhang in topology optimization for additive manufacturing. *Struct Multidiscip Optim* 60(1):59-67. <https://doi.org/10.1007/s00158-019-02194-x>
- van de Ven, E, Maas, R, Ayas, C, Langelaar, M, van Keulen, F (2020) Overhang control based on front propagation in 3D topology optimization for additive manufacturing. *Comput Methods Appl Mech Eng* 369:1-21. <https://doi.org/10.1016/j.cma.2020.113169>
- Wang, C (2022) Simultaneous optimization of build orientation and topology for self-supported enclosed voids in additive manufacturing. *Comput Methods Appl Mech Eng* 388:114227. <https://doi.org/https://doi.org/10.1016/j.cma.2021.114227>
- Wang, C, Zhu, J, Zhang, W (2022) Simultaneous optimization of structural topology and build direction using B-spline parameterized density method. *Struct Multidiscip Optim* 65(11):313. <https://doi.org/10.1007/s00158-022-03422-7>
- Wang, CF, Qian, XP (2020) Simultaneous optimization of build orientation and topology for additive manufacturing. *Addit Manuf* 34:1-19. <https://doi.org/10.1016/j.addma.2020.101246>
- Wang, FW, Lazarov, BS, Sigmund, O (2011) On projection methods, convergence and robust formulations in topology optimization. *Struct Multidiscip Optim* 43(6):767-784. <https://doi.org/10.1007/s00158-010-0602-y>
- Wang, YG, Gao, JC, Kang, Z (2018) Level set-based topology optimization with overhang constraint: Towards support-free additive manufacturing. *Comput Methods Appl Mech Eng* 339:591-614. <https://doi.org/10.1016/j.cma.2018.04.040>
- Xu, B, Han, YS, Zhao, L, Xie, YM (2020) Topological optimization of continuum structures for additive manufacturing considering thin feature and support structure constraints. *Eng Optim* 53(12):2122-2143. <https://doi.org/10.1080/0305215x.2020.1849170>

Yang, RJ, Chuang, CH, Che, XD, Soto, C (2000) New applications of topology optimization in automotive industry. *Int J Veh Des* 23(1-2):1-15. <https://doi.org/10.1504/ijvd.2000.001878>

Zhang, KQ, Cheng, GD, Wang, Y (2022) Structural topology optimization subject to overhang angle constraint with overhang length relaxation in additive manufacturing. *Sci China Technol Sci* 65(6):1213-1231. <https://doi.org/10.1007/s11431-021-1996-y>

Zhang, KQ, Cheng, GD, Xu, L (2019) Topology optimization considering overhang constraint in additive manufacturing. *Comput Struct* 212:86-100. <https://doi.org/10.1016/j.compstruc.2018.10.011>

Zhang, WH, Zhou, L (2018) Topology optimization of self-supporting structures with polygon features for additive manufacturing. *Comput Methods Appl Mech Eng* 334:56-78. <https://doi.org/10.1016/j.cma.2018.01.037>

Zhang, YC, Bernard, A, Harik, R, Karunakaran, KP (2017) Build orientation optimization for multi-part production in additive manufacturing. *J Intell Manuf* 28(6):1393-1407. <https://doi.org/10.1007/s10845-015-1057-1>

Zhou, Y, Nomura, T, Saitou, K (2019) Multicomponent Topology Optimization for Additive Manufacturing With Build Volume and Cavity Free Constraints. *J Comput Inf Sci Eng* 19(2). <https://doi.org/10.1115/1.4042640>

Zhu, JH, Zhang, WH, Xia, L (2016) Topology Optimization in Aircraft and Aerospace Structures Design. *Arch Comput Methods Eng* 23(4):595-622. <https://doi.org/10.1007/s11831-015-9151-2>

Zou, J, Zhang, YC, Feng, ZY (2021) Topology optimization for additive manufacturing with self-supporting constraint. *Struct Multidiscip Optim* 63(5):2341-2353. <https://doi.org/10.1007/s00158-020-02815-w>